Deep-Sea Research I 58 (2011) 590–614

Contents lists available at ScienceDirect

Deep-Sea Research I

journal homepage: www.elsevier.com/locate/dsri

The Irminger Gyre: Circulation, convection, and interannual variability

Kjetil Våge [a,*,1], Robert S. Pickart [a], Artem Sarafanov [b], Øyvind Knutsen [c], Herlé Mercier [d], Pascale Lherminier [d], Hendrik M. van Aken [e], Jens Meincke [f], Detlef Quadfasel [f], Sheldon Bacon [g]

[a] Woods Hole Oceanographic Institution, Woods Hole, USA
[b] P.P. Shirshov Institute of Oceanology, Moscow, Russia
[c] SINTEF Fisheries and Aquaculture, Trondheim, Norway
[d] Laboratoire de Physique des Océans, Plouzané, France
[e] Royal Netherlands Institute for Sea Research, Den Burg, Netherlands
[f] Institut für Meereskunde, Universität Hamburg, Hamburg, Germany
[g] National Oceanography Centre, Southampton, UK

ARTICLE INFO

Article history:
Received 1 July 2010
Received in revised form
25 February 2011
Accepted 3 March 2011
Available online 21 March 2011

Keywords:
Irminger Sea
Labrador Sea Water
Deep Western Boundary Current
Irminger Current
North Atlantic
Deep convection

ABSTRACT

In this study 36 hydrographic transects occupied between 1991 and 2007 in the vicinity of the WOCE A1E/AR7E section are used to investigate various aspects of the Irminger Gyre, a narrow cyclonic recirculation in the southwest Irminger Sea. Vertical sections of absolute geostrophic velocity were constructed using satellite and shipboard velocity measurements, and analyzed in conjunction with the hydrographic data and meteorological fields. The Irminger Gyre is a weakly baroclinic feature with a mean transport of 6.8 ± 1.9 Sv ($1\ \text{Sv} = 10^6\ \text{m}^3/\text{s}$). At mid-depth it contains water with the same properties as Labrador Sea Water (LSW). During the 17-year study period large changes occurred in the gyre and also within the boundary flow encircling the Irminger Sea. The gyre intensified and became more stratified, while the upper-layer circulation of the boundary current system weakened. The latter is consistent with the overall decline of the North Atlantic subpolar gyre reported earlier. However, the decline of the upper-ocean boundary currents was accompanied by an intensification of the circulation at deeper levels. The deep component of both the northward-flowing boundary current (the Irminger Current) and the southward-flowing boundary current (the Deep Western Boundary Current) strengthened. The increase in transport of the deep Irminger Current is due to the emergence of a second deep limb of the current, presumably due to a shift in pathways of the branches of the subpolar gyre. Using a volumetric water mass analysis it is argued that LSW was formed locally within the Irminger Gyre via deep convection in the early 1990s. In contrast, LSW appeared outside of the gyre in the eastern part of the Irminger Sea with a time lag of 2–3 years, consistent with transit from the Labrador Sea. Thus, our analysis clarifies the relative contributions of locally-versus remotely-formed LSW in the Irminger Sea.

1. Introduction

From a climatic perspective, the Irminger Sea is a region of particular importance (Fig. 1). Here a large fraction of the freshwater export from the Arctic first meets the subpolar North Atlantic (Dickson et al., 2007), the dense overflows from the Nordic seas merge to form the Deep Western Boundary Current (DWBC, Dickson and Brown, 1994), and wintertime convection is thought to form Labrador Sea Water (LSW) outside of the Labrador Basin (Pickart et al., 2003b). To some extent these phenomena are linked. Freshwater from the Arctic carried into the Irminger Sea along the coast of Greenland can be fluxed offshore by winds or instabilities (Pickart et al., 2005) or be retroflected off the Greenland shelf (Holliday et al., 2007) and impact the ventilation process in the interior basin. This in turn can influence the properties of the intermediate water masses entrained into the DWBC (Yashayaev, 2007). It is important to elucidate these different processes and their precise relationship to each other, which will ultimately allow us to understand better the Irminger Sea's role in the complex North Atlantic climate system.

Although the general circulation of the Irminger Sea has been fairly well described, important aspects of both the boundary current system and the interior flow remain unclear. On the eastern side of the Irminger Sea Atlantic-origin water is carried

* Corresponding author.
E-mail address: kjetil.vage@gfi.uib.no (K. Våge).
[1] Now at Geophysical Institute, University of Bergen, Bergen, Norway.

0967-0637/$ - see front matter © 2011 Elsevier Ltd. All rights reserved.
doi:10.1016/j.dsr.2011.03.001

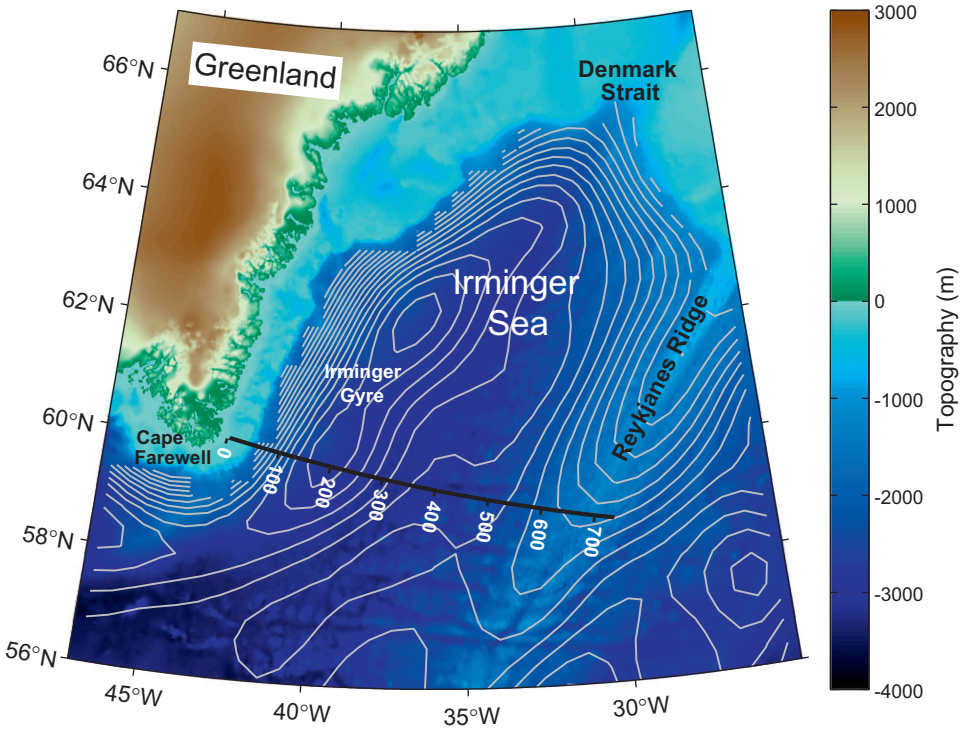

Fig. 1. Topography (color) of southeast Greenland and the Irminger Sea from the Etopo2 2-minute elevation data base. The black line identifies the least squares regression line onto which all in-situ data have been projected (see Section 2) and the white numbers indicate distance (in km). The gray lines are contours of objectively mapped geostrophic pressure at 700 db, from Lavender et al. (2000). The closed contours in the western Irminger Sea reveal the location of the Irminger Gyre. (For interpretation of the references to color in this figure legend, the reader is referred to the web version of this article.)

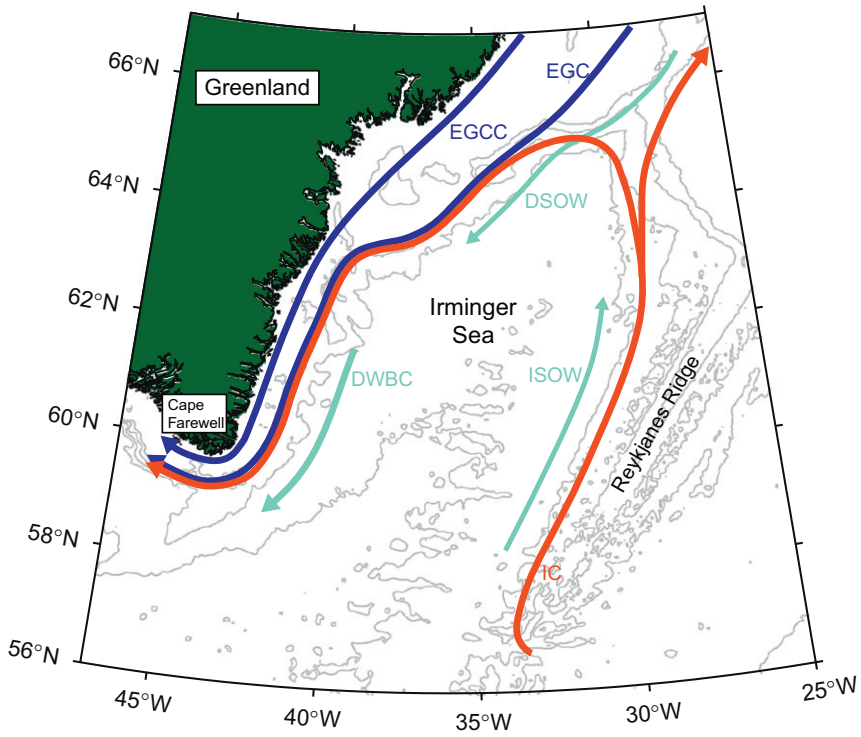

Fig. 2. The boundary currents of the Irminger Sea. The acronyms are: IC=Irminger Current; EGC=East Greenland Current; EGCC=East Greenland Coastal Current; DWBC = Deep Western Boundary Current; DSOW=Denmark Strait Overflow Water; ISOW = Iceland Scotland Overflow Water. Red (blue) arrows indicate upper-layer transport of warm (cold) water, while green arrows denote deep currents. The 500, 1000, 1500, 2000, and 3000 m isobaths are plotted. (For interpretation of the references to color in this figure legend, the reader is referred to the web version of this article.)

northwards by the Irminger Current along the flank of the Reykjanes Ridge (Fig. 2). Little is known about the velocity structure of this current or its variability. South of the Denmark Strait the Irminger Current bifurcates: One branch continues northward through the strait, while the major fraction recirculates to the south. Along the western boundary a series of swift

currents flow equatorward along the shelf and slope. On the inner shelf the East Greenland Coastal Current advects a combination of coastal runoff and Arctic-origin water (Bacon et al., 2002; Sutherland and Pickart, 2008), while at the shelfbreak the cold, fresh East Greenland Current flows alongside the retroflected portion of the warm, salty Irminger Current. Recently a narrow, intense jet of dense water has been measured on the upper slope (beneath the Irminger Current), referred to as the East Greenland Spill Jet (Pickart et al., 2005). It remains unclear how these different flow components merge to form the single shelfbreak jet found downstream at Cape Farewell (the southern tip of Greenland). Farther down the continental slope the DWBC advects overflow water from the Nordic seas to the south.

The circulation in the interior Irminger Basin is even less certain. While it has been known for over a century that the general sense of the flow is cyclonic (Knudsen, 1899), direct measurements were obtained only recently by Lavender et al. (2000) who mapped the subsurface flow using float trajectories. Their results revealed the presence of a relatively narrow recirculation gyre in the western part of the basin (Fig. 1). We refer to this feature as the Irminger Gyre. Because of its predominantly barotropic nature and lack of geostrophic shear, the gyre is difficult to detect in hydrographic data. Hence, even basic characteristics such as its transport, vertical structure, and variability are unknown. The float data of Lavender et al. (2000) suggest that the Irminger Gyre is part of a larger band of low geostrophic pressure that extends around Cape Farewell into the southeast Labrador Sea (Fig. 1). The flow on the seaward side of this band represents a pathway for LSW to travel from the Labrador Sea to the Irminger Sea (Talley and McCartney, 1982; Straneo et al., 2003; Faure and Speer, 2005).

The Irminger Sea lies beneath the North Atlantic storm track, and consequently the atmospheric forcing in the basin is strongly influenced by the passage of low pressure systems. In general, the North Atlantic Oscillation (NAO) dictates the number and strength of the storms that pass through the area: A positive NAO state is characterized by stronger westerly winds, an increased occurrence and magnitude of cyclones, and a northeastward shift in the storm track (e.g. Rogers, 1990). However, the high topography of Greenland strongly modulates the local air-sea forcing. In the vicinity of Cape Farewell intense, small-scale wind events known as westerly tip jets develop as the cyclones pass to the northeast (Doyle and Shapiro, 1999; Moore and Renfrew, 2005; Våge et al., 2009b). These are predominantly a wintertime phenomenon, and a greater (smaller) number of events tends to occur when the NAO index is high (low) and the Icelandic low is shifted towards the north (south) (Bakalian et al., 2007; Våge et al., 2009b). Mean wind speeds up to 30 m/s generating heat fluxes approaching 600 W/m^2 are generally sustained for less than a day, but many such tip jet events can occur over the course of a winter (on average 13 ± 5 events, Våge et al., 2009b).

Westerly tip jets have been linked with the oceanic circulation in the Irminger Sea (Pickart et al., 2003a; Spall and Pickart, 2003). Spall and Pickart (2003) noted that the strong wintertime wind stress curl east of Greenland (see also Chelton et al., 2004) would induce upwelling, consistent with a cyclonic recirculation. The enhanced wind stress curl is mainly caused by the sharp northward gradient in zonal wind speed associated with the tip jet (Pickart et al., 2003a). Using an idealized hydrostatic, primitive equation general circulation model (GCM) driven by such a wintertime wind stress curl pattern, Spall and Pickart (2003) reproduced many of the circulation features observed by Lavender et al. (2000, 2005), including the Irminger Gyre. The circulation persisted throughout the summer – when the wind forcing was absent – maintained by a combination of weak stratification and sloping bathymetry under the forcing region. Hence there was only a weak seasonality of the Irminger Gyre despite a strong seasonal modulation of the winds. Spall and Pickart (2003) argue that baroclinic Rossby waves interact with the bottom and slow the circulation during winter when the forcing is present, and maintain the circulation during the rest of the year when there is no forcing. An earlier model study by Käse et al. (2001) suggests that wind forcing, bathymetry and the Denmark Strait overflow all play important roles for the mid-depth recirculations in the Labrador and Irminger seas.

It has been argued that LSW can be formed in the southwest Irminger Sea due to convection triggered by the westerly tip jet events. Using historical hydrography and a numerical model, Pickart et al. (2003b) explained the existence of an isolated region of weak mid-depth stratification to the east of Cape Farewell. Våge et al. (2008) elucidated the effects of the tip jets on the seasonal evolution of the mixed-layer using mooring data in the central Irminger Sea and a 1-D mixed-layer model. More recently, direct observations of deep mixed layers in the Irminger Sea were obtained during the winter of 2007–2008 from Argo float profiles (Våge et al., 2009a) and moored time series (de Jong, 2010). Despite this mounting evidence, the notion of deep convection in the Irminger Sea has been questioned. For example, it was argued that the weakly stratified intermediate water found in the Irminger Sea is predominantly advected from the Labrador Sea on a relatively short time scale (approximately 2 years, see Yashayaev et al., 2007a) and that a continuously present intermediate salinity maximum across the Irminger Basin indicates that there was no significant formation of LSW in the Irminger Sea after 1991 (Bersch et al., 2007).

Over the last two decades significant and well-documented changes have taken place in the subpolar North Atlantic, influenced largely by the NAO. The late 1980s and early 1990s were characterized by an especially high NAO index, and the coldest and densest LSW on record was formed during this period (Yashayaev, 2007). In the winter of 1995–1996 the NAO index dropped precipitously and has not fully returned to its previous levels. The consequent decrease in wind and air-sea buoyancy forcing led to a significant reduction of deep LSW formation (Lazier et al., 2002; Avsic et al., 2006; Yashayaev, 2007). At the same time the subpolar gyre circulation has slowed and contracted (Häkkinen and Rhines, 2004; Hátún et al., 2005; Bersch et al., 2007; Sarafanov et al., 2008). The sea surface height analysis by Häkkinen and Rhines (2004) revealed that the strongest signal associated with this interannual variability was located in the Irminger Sea. It has recently been demonstrated (Sarafanov, 2009; Sarafanov et al., 2010b) that an increasing influence of warm and salty subtropical waters on the eastern North Atlantic associated with the contraction of the gyre has reversed the intermediate and deep freshening trend of the preceding 3–4 decades (Dickson et al., 2002; Curry et al., 2003). Furthermore, using altimetry and repeat hydrography, Sarafanov et al. (2009, 2010a) inferred that the decline of the upper-ocean western boundary current in the Irminger Sea in the 1990s and 2000s was accompanied by an increase in the deep water transport.

Due to its central role in the circulation of the western subpolar gyre and its potential importance to the occurrence of convection in the Irminger Sea, the Irminger Gyre warrants further study. If there is a second site of LSW formation, outside of the Labrador Basin, this would have important ramifications for our understanding of the North Atlantic Meridional Overturning Circulation, the modification of the dense overflow waters from the Nordic seas, and the stratification and ventilation of the interior North Atlantic. This forms the motivation for the present study. Our main objectives are to (i) quantify the structure, transport and interannual variability of the Irminger Gyre and

(ii) investigate the importance of the Irminger Sea as a source region for LSW. We use a collection of hydrographic transects across the southern Irminger Sea, along with satellite and shipboard velocity measurements and meteorological fields. The data sets and methods are presented in Section 2. We describe the mean state and interannual variability of the Irminger Sea in Sections 3 and 4. Transports across the basin (Fig. 1) are quantified in Section 5. Finally, we distinguish the presence of locally versus remotely formed LSW in the Irminger Sea in Section 6, which clarifies our understanding of the contributions of the Labrador and Irminger basins in ventilating the mid-depth North Atlantic.

2. Data and methods

2.1. Hydrography

Since 1991, hydrographic transects in the vicinity of the World Ocean Circulation Experiment (WOCE) A1E/AR7E section across the southern Irminger Sea between Greenland and the Reykjanes Ridge (Fig. 3) have been occupied up to several times every year, with the exceptions of 1993 and 1998. Table 1 and Fig. 4 list all 36 occupations. Apart from the April 1991 and November 1994 transects, all of the sections were conducted during the summer half-year period of May through October (hereafter referred to as summer), mainly between June and August (69% of the sections). The hydrographic data generally meet the standards described in the WOCE operations manual (accuracies of 0.002 °C, 0.002 and 3 db for temperature, salinity, and pressure, respectively).

2.2. Shipboard velocities

The container vessel Nuka Arctica operates on a three-week schedule from spring to fall between Denmark and Greenland. In 1999 it was outfitted with a 150 kHz acoustic Doppler current profiler (ADCP). The objective was to obtain enough observations of the upper-ocean circulation in the northeast subpolar Atlantic to construct robust ensemble averages, thereby permitting investigation of the total velocity field and its variability (Knutsen et al., 2005). From 1999 to 2002 nearly 50 crossings took place during the months of April–December (Fig. 5), with the majority of them occurring between June and August (52% of the transects). The data have been manually edited and de-tided. The Nuka Arctica continued to record

Table 1
Hydrographic transects across the southern Irminger Sea used in the study.

Date	Principal investigator	Ship/Country
Apr 1991	van Aken	Tyro/NL
Aug 1991	Gould	Charles Darwin/GB
Sep 1991	Meincke	Meteor/DE
Sep 1992	Sy	Valdivia/DE
Nov 1994	Meincke	Meteor/DE
Jun 1995	Bersch	Valdivia/DE
Aug 1996	Bersch	Valdivia/DE
Oct 1996	Bacon	Discovery/GB
Aug 1997	Sy	Meteor/DE
Oct 1997	Sokov	Professor Shtokman/RU
May 1999	Bersch	Valdivia/DE
Aug 1999	Meincke	Meteor/DE
Aug 2000	Hübner	Poseidon/DE
Oct 2000	van Aken	Pelagia/NL
Jun 2001	Holfort	Meteor/DE
Aug 2001	Pickart	Oceanus/US
Jun 2002	Holfort	Poseidon/DE
Jun 2002	Mercier	Thalassa/FR
Jul 2002	Bersch	Alexander von Humboldt/DE
Aug 2002	Morozov	Akademik Mstislav Keldysh/RU
Aug 2002	Pickart	Oceanus/US
Jul 2003	Mortensen	Meteor/DE
Jul 2003	Sokov	Akademik Ioffe/RU
Jul 2003	Pickart	Oceanus/US
Sep 2003	van Aken	Pelagia/NL
Jun 2004	Huck	Thalassa/FR
Jun 2004	Pisarev	Akademik Ioffe/RU
Jul 2004	Pickart	James Clark Ross/GB
Aug 2004	Quadfasel	Alexander von Humboldt/DE
Jun 2005	Pisarev	Akademik Ioffe/RU
Sep 2005	Bacon	Discovery/GB
Sep 2005	van Aken	Pelagia/NL
Jun 2006	Lherminier	Maria S. Merian/FR
Jul 2006	Sokov	Akademik Ioffe/RU
Aug 2006	Bacon	Discovery/GB
Jul 2007	Sokov	Akademik Ioffe/RU

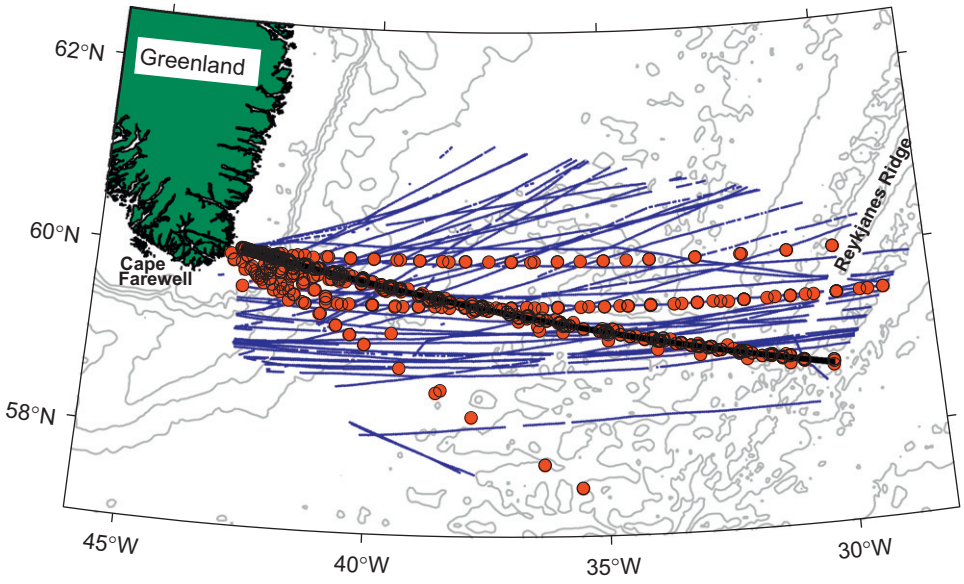

Fig. 3. In-situ data used in the study. The black line identifies the least squares regression line onto which the data have been projected. The red circles and blue dots mark locations of hydrographic and direct velocity measurements, respectively. Every 500 m isobath is contoured. (For interpretation of the references to color in this figure legend, the reader is referred to the web version of this article.)

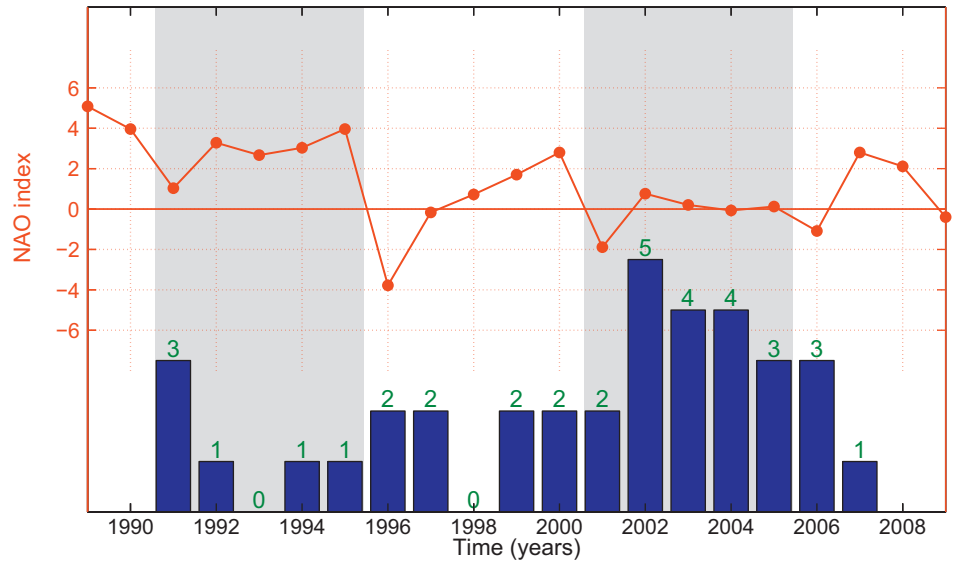

Fig. 4. Number of hydrographic sections per year (blue bars) and December–March NAO index from (Hurrell, 1995 [red]). The gray shading highlights the 1991–1995 and 2001–2005 pentads. (For interpretation of the references to color in this figure legend, the reader is referred to the web version of this article.)

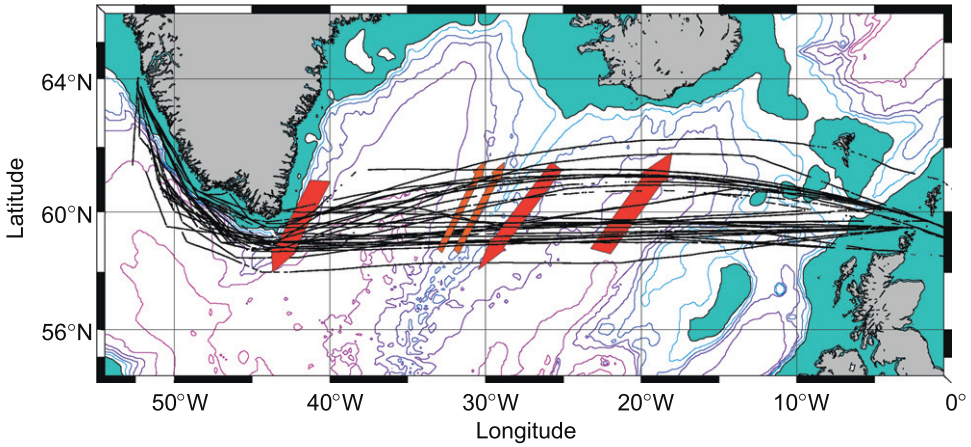

Fig. 5. Nuka Arctica transects between 1999 and 2002. The green areas are shallower than 500 m, and depth is contoured with 500 m increments. The arrows represent from west to east: The EGC, two peaks of the IC (discussed further below), southward flow on the eastern side of the Reykjanes Ridge, and the North Atlantic Current. (For interpretation of the references to color in this figure legend, the reader is referred to the web version of this article.) From Knutsen et al. (2005). © 2011 American Geophysical Union. Reproduced/modified by permission of American Geophysical Union.

ADCP data beyond 2002, but problems with the logging system have prevented the data set from being updated (T. Rossby, personal communication, 2009). Additionally, for three of the hydrographic transects occupied between 1999 and 2002, concurrent shipboard ADCP measurements were obtained.

2.3. Satellite altimetry

In this study we use absolute dynamic ocean topography (DOT) and geostrophic velocities provided by Archiving, Validation, and Interpretation of Satellite Oceanographic data (AVISO). Since October 1992, sea surface height (SSH) anomalies from multiple satellite altimeter missions have been consistently combined using state-of-the-art merging techniques and mapped onto a 1/3° grid at weekly temporal resolution (Ducet et al., 2000; Le Traon et al., 2003). Standard corrections to the altimeter data to take into account instrument noise, orbit error, atmospheric attenuation, sea state bias, and tides were applied by AVISO. Absolute dynamic topography was obtained from a combination of the SSH anomalies and a mean dynamic topography product, which was computed from altimetry, in-situ data, and a geoid model (Rio and Hernandez, 2004). Due to land contamination effects, the presence of ice, errors in the tide model, and limitations of the geoid estimate, the absolute dynamic topography is not expected to be very accurate near the coast or on lateral scales shorter than about 200 km (R. Ponte, personal communication, 2009). Limitations and error estimates associated with the use of the AVISO data set in the present analysis are discussed below.

2.4. Atmospheric reanalysis

Monthly mean wind vectors and latent and sensible heat fluxes were obtained from the high-resolution North American Regional Reanalysis project (NARR, Mesinger et al., 2006). From the monthly mean winds we computed wind stress curl using the method of Milliff and Morzel (2001). The spatial resolution of the NARR fields is 32 km. The increased resolution relative to the

global reanalysis products (e.g. NCEP) is important for a more realistic rendition of the tip jet (Jung and Rhines, 2007).

2.5. Projection and gridding

In order to facilitate the analysis and enable the use of quantitative techniques such as empirical orthogonal functions (EOFs), the hydrographic sections were interpolated onto a standard grid in the distance-depth plane. This was accomplished as follows. A least squares regression line was fit through the locus of the hydrographic station positions (stations from the zonal and pronouncedly southward sections were excluded). As the majority of the sections closely followed the WOCE A1E/AR7E line, the regression line is nearly identical to the WOCE line. The regression line will hereafter be referred to simply as AR7E. A bathymetry profile along AR7E was extracted from Etopo2 (Fig. 1). A second bathymetry profile was estimated from the maximum depth of each station under the assumption that the measurements ended 10 m above the bottom (e.g. Pickart, 2004). Overall there was very good agreement between the two resulting depth curves. The final bathymetry profile is a smoothed combination of the Etopo2 and station-based depth estimates, with the deeper profile chosen at each location.

Each station was subsequently projected onto the AR7E line. To the west of the center of the Irminger Basin the location of each station along AR7E was tentatively determined by minimizing the distance between its original position and the AR7E line. In the cases where the discrepancy between the station's original and projected depths exceeded a tolerance criterion (5%), the projected location was moved along the AR7E line until its original depth matched the bathymetry profile within the set tolerance. In the eastern part of the Irminger Basin the northward shoaling of the Reykjanes Ridge towards Iceland presented a complication. The topography of the Reykjanes Ridge has an important dynamical effect on the flow (see for instance Fig. 5), and inspection of the mean AVISO absolute surface velocities shows that in the vicinity of the AR7E line the flow is largely parallel to the ridge. Hence it was decided that the distance of each station from the center of the Reykjanes Ridge should be maintained under the projection. Accordingly, in the eastern part of the Irminger Basin each station was first projected onto the AR7E line such that the projected distance was minimized. Subsequently the station was adjusted along the line until its distance from the center of the ridge was preserved. The requirement of conservation of distance from the ridge was linearly relaxed between the center of the basin and the ridge such that the projection was completely determined by distance from the ridge near the ridge and completely determined by minimum projected distance near the center of the basin.

In total, 658 stations from the 36 sections were projected onto the AR7E line. In the same fashion each ADCP measurement was also projected onto the AR7E line. The only difference between these procedures was that the original bottom depth of each ADCP measurement was solely determined by Etopo2. Measurements from locations requiring a projection in excess of 200 km were discarded. As most of the hydrographic stations were located in the vicinity of AR7E, the distance of projection was less than 5 km for 69% of the stations and only 18% of the stations were moved more than 25 km from their original locations. In summary, measurements from the western side of the Irminger Basin were projected along isobaths onto the AR7E line, while in the eastern half of the basin the distance from the Reykjanes Ridge was also taken into account.

The hydrographic and direct velocity data from individual projected sections were then interpolated onto a standard 5 km by 10 m grid using a Laplacian-spline interpolator (see Pickart and Smethie, 1998, for details of this procedure). The western half of the Irminger Basin was sampled during the majority of the occupations, while hydrographic measurements were conducted across the entire basin from the Greenland shelf to the Reykjanes Ridge during 70% of the occupations. The collection of gridded sections is used as the working data set throughout the rest of the study.

2.6. ADCP-referenced geostrophic velocities

Geostrophic velocities along the AR7E section were referenced two ways: Using the shipboard ADCP velocity data in the upper part of the water column, and using the AVISO gridded surface velocities. Since the time period covered by AVISO (1993–2007) is much greater than that sampled by the Nuka Arctica container vessel (1999–2002), in order to meaningfully investigate interannual variability it is necessary to use the former product. As such, the ADCP-referenced absolute velocities were used primarily to assess the accuracy of the AVISO-referenced velocities.

For the Nuka Arctica time period, a weighted mean ADCP section over the depth interval 50 to 350 m was computed. The weights are inversely proportional to the distance of projection (projection distances shorter than 25 km were given equal weight). The weighting scheme was implemented because of the change in direction of the current flowing along the western boundary as it starts to curve around Cape Farewell, and the Greenland slope is also the only region where the weighted and unweighted mean vertical ADCP sections differed significantly (not shown). The absolutely-referenced geostrophic flow was computed following the procedure of Pickart et al. (2005). In particular, each of the 11 gridded vertical sections of temperature and salinity for the Nuka Arctica time period 1999–2002 was used to calculate the dynamic height, from which relative geostrophic velocities were computed. The individual sections were then re-mapped onto the standard grid and averaged to create a mean thermal wind section. Finally, this section was referenced by matching the vertically averaged relative and ADCP velocities at each horizontal grid point. Although the de-tided ADCP velocity field still contains ageostrophic motions, good agreement between the mean ADCP and the mean absolute geostrophic velocities (not shown) indicate that the ageostrophic components were largely averaged out and had little influence on the result. Below we compare the near-surface ADCP-referenced geostrophic velocities to the AVISO product for the 4-year period of overlap.

2.7. AVISO-referenced geostrophic velocities

The mean absolute geostrophic velocities computed above from the subset of 11 hydrographic and 47 direct velocity sections provide a realistic estimate of the flow across the AR7E line during the 1999–2002 time period. However, to examine the evolution of the flow throughout the entire period (1991–2007), additional reference velocity information is needed. Global sea surface height has continuously been measured by multiple satellite altimeters since October 1992. We examined the merged AVISO geostrophic surface velocity product to see how it compares against our independently computed ADCP-referenced surface geostrophic velocities. The mean 1999–2002 AVISO surface velocity field (for the months of April through December, to coincide with the period of hydrographic and direct velocity measurements) was interpolated onto the AR7E line and the velocity component normal to AR7E determined. The comparison between the AVISO and ADCP-referenced surface velocities is shown in Fig. 6(a). Although the AVISO curve is smoother, the

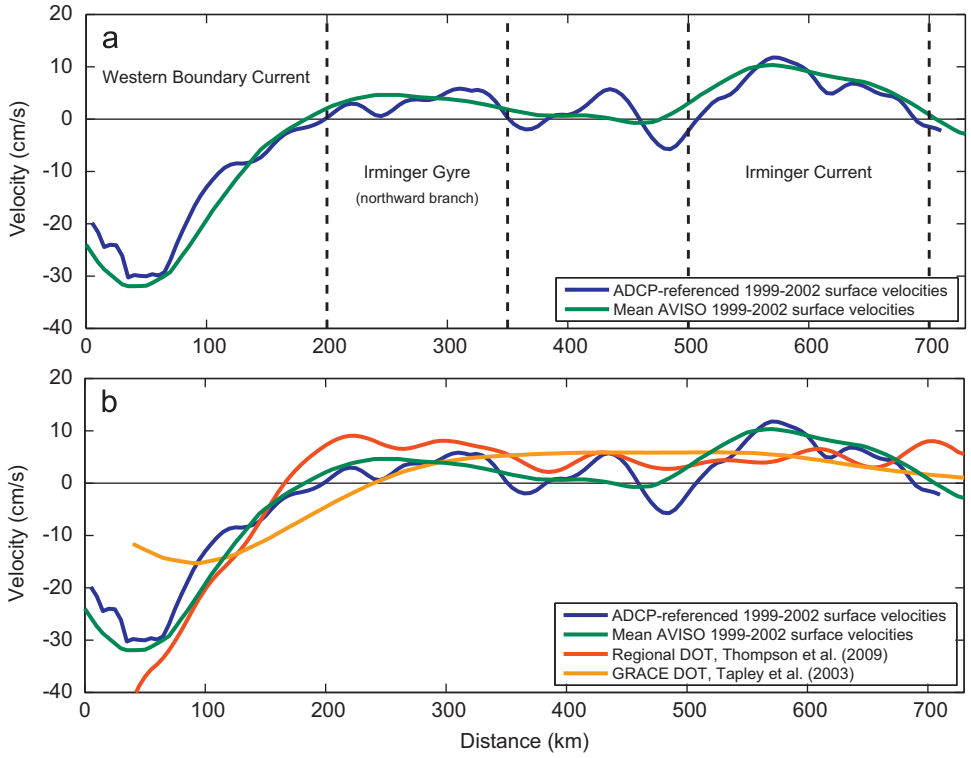

Fig. 6. Comparison of surface velocities across the AR7E line. (a) The blue line is a trace of the mean 1999–2002 near-surface ADCP-referenced absolute geostrophic velocities (10–50 m vertically averaged). The green line shows the mean 1999–2002 AVISO surface velocities. The approximate locations of the primary circulation features (discussed in the text) are indicated. (b) The additional red and orange lines are mean surface velocities computed from the dynamic ocean topographies (DOTs) of Thompson et al. (2009) and Tapley et al. (2003), respectively. (For interpretation of the references to color in this figure legend, the reader is referred to the web version of this article.)

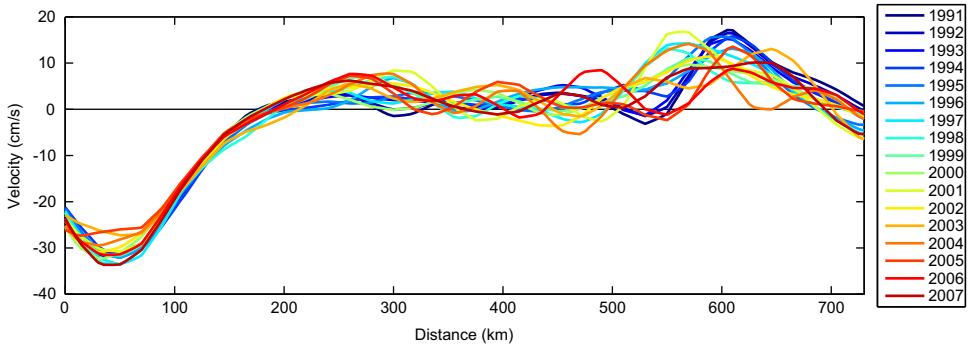

Fig. 7. Annually (May–Oct) averaged (1993–2007) and extrapolated (1991–1992) AVISO reference velocity curves. (For interpretation of the references to color in this figure legend, the reader is referred to the web version of this article.)

agreement between the two independent products is striking, with a root-mean-square (RMS) deviation of less than 3.0 cm/s. Both curves display the primary circulation features of the Irminger Sea: The Western Boundary Current (WBC, approximately 0–200 km), the northward branch of the Irminger Gyre (IG, approximately 200–350 km), and the Irminger Current (IC, approximately 500–700 km). We note that the AVISO product has smoothed out the two surface peaks of the IC that were discussed by Knutsen et al. (2005) using the Nuka Arctica ADCP data alone.

Two other surface velocity curves computed from independent mean DOT products were evaluated for possible use as reference velocities with the geostrophic calculation (Fig. 6(b)). These would need to be coupled to the AVISO velocity anomaly fields in order to provide time-varying reference information. The GRACE-based DOT estimate of Tapley et al. (2003, orange line) is best suited for applications with wavelengths greater than 500 km, and does not properly resolve the scales of interest in this study. Thompson et al. (2009) used terrestrial and altimeter-derived gravity data to add high wave number detail to their regional DOT of the northwest Atlantic. They were able to resolve oceanographic features with length scales of order 100 km such as the Mann Eddy. An updated version of their DOT (red line, S. Higginson, personal communication, 2010) does capture the primary features of interest in the Irminger Sea (the WBC, the IG, and the IC). However, the magnitude of the surface

flow in the WBC is too high, while the IC is too weak and its peak is displaced to the east by about 100 km compared to our ADCP-referenced geostrophic surface velocities (Fig. 6(b)). Despite the above mentioned shortcomings (lack of accuracy for flow on the shelf and on short spatial scales), the AVISO absolute geostrophic surface velocities calculated using the DOT of Rio and Hernandez (2004) are obviously the best choice at present for referencing our geostrophic velocity sections over the full time period (the Greenland shelf area will not be included in our transport estimates).

In order to investigate the time-varying nature of the flow in the Irminger Sea, we chose to consider annual averages, or, more precisely, summer averages (May through October). The rationale was to reduce the effects of mesoscale activity as well as altimeter data uncertainty, and the majority of the hydrographic sections were occupied during these months. Accordingly, a single composite AVISO velocity curve was computed for each year (May–Oct.) for the period 1993–2007 (Fig. 7). These surface velocity curves were then used to reference the annually-averaged thermal wind sections calculated from the AR7E occupations throughout the rest of the study. AVISO only extends back to October 1992, which is not sufficient to provide reference velocity information for the 1991 and 1992 hydrographic sections. However, the early 1990s was a period of uniformly strong atmospheric forcing, as witnessed by the consistently high NAO index (Fig. 4), and, perhaps not surprisingly, there was little difference in the reference velocity curves from 1993 to 1996. This provided justification to extend the timeseries back in time to 1991 via linear extrapolation, under the assumption that the circulation in 1991 and 1992 was similar in character to the succeeding years (Fig. 7).[2] This is admittedly a big assumption, and the resulting transport estimates for 1991 and 1992 should be considered as less certain. Error estimates for the absolute geostrophic velocities are presented in the appendix.

3. Mean structure

We first examine the overall (1991–2007) mean hydrographic and absolute geostrophic velocity fields, which are displayed in Fig. 8. Following previous studies (e.g. Holliday et al., 2009) we partition the water column into shallow, intermediate, and deep water masses.

Throughout most of the shallow layer ($\sigma_\theta < 27.70$ kg/m^3) is a warm, saline Atlantic-origin water mass called Irminger Sea Water that is mainly supplied by the Irminger Current. The IC is a branch of the North Atlantic Current that enters the Irminger Sea as a northward flow along the western side of the Reykjanes Ridge. In the mean it is a surface-intensified flow roughly 200 km wide, with a deep extension reaching the 1500 m isobath (Fig. 8(c)). The major fraction of the IC (up to 85%, Pickart et al., 2005) flows around the Irminger Basin (Fig. 2) and continues south along the Greenland slope. Here a sharp hydrographic front separates the Irminger Sea Water from the cold, fresh Arctic-origin water carried by the East Greenland Current. From velocity alone we are unable to distinguish the boundary between the southward flow of the East Greenland Current and that of the IC. This was the case as well in studies farther to the south (Fratantoni and Pickart, 2007). We will hereafter refer to the combined southward flow along the Greenland slope as the Western Boundary Current and the northward flow along the Reykjanes Ridge as the Irminger Current.

[2] Though the atmospheric state had shifted by 1996, the surface circulation had not yet adjusted to make it significantly different from the preceding years, and it was included as the most recent end point of the extrapolation.

The intermediate layer (27.70 kg/m$^3 < \sigma_\theta < 27.80$ kg/m^3) is dominated by Labrador Sea Water, which is identifiable by a mid-depth minimum of salinity and potential vorticity (e.g. Talley and McCartney, 1982). The low potential vorticity signifies weak stratification, which may be traced to the convective origin of LSW. The most pure LSW in the Irminger Sea is found in the western half of the basin (note the doming and deepening 27.70 and 27.80 kg/m^3 isopycnals, respectively). The warmer and saltier water mass occupying the same depth as LSW in the vicinity of the Reykjanes Ridge is called Icelandic Slope Water (van Aken and de Boer, 1995; Read, 2001).

Two distinct water masses are found in the deep layer ($\sigma_\theta > 27.80$ kg/m^3), both of which contribute to the DWBC and originate from the dense Nordic seas overflows. Near the bottom, the cold and fresh signature of the Denmark Strait Overflow Water (DSOW) is evident. Directly above this the Iceland–Scotland Overflow Water (ISOW) is identifiable by the deep salinity maximum. This water mass is often referred to as North East Atlantic Deep Water, and its greater salinity results largely from entrainment of saline Atlantic-origin waters primarily in the vicinity of the Iceland–Scotland sills (Fogelqvist et al., 2003). The boundary separating ISOW and DSOW is usually taken to be the 27.88 kg/m^3 isopycnal (e.g. Dickson and Brown, 1994), and we adopt this definition as well. Collectively, DSOW, ISOW, and entrained LSW form the major fraction of the DWBC, and are referred to as North Atlantic Deep Water (NADW), a water mass that constitutes a significant fraction of the World Ocean (Johnson, 2008) and plays an important role in the Meridional Overturning Circulation.

The largest velocities in the mean section are found in the boundary current system. The IC flows northward on the western side of the Reykjanes Ridge, and returns as a surface-intensified flow in the upper part of the WBC. The enhanced southward flow at the bottom of the WBC is the DSOW, which has a "tail" extending offshore to roughly the 3000 m isobath. This feature is seen in synoptic sections as well (Pickart et al., 2005). As previously noted (e.g. Lherminier et al., 2010), in the central Irminger Basin there is little density shear throughout most of the water column, which results in a largely depth-independent flow. The northward flow of the Irminger Gyre is clearly evident in the mean section, consistent with current meter data collected at this location (Våge et al., 2008). We defined the southward limb of the gyre as the seaward part of the WBC necessary to balance the northward transport at each density level in the water column. The boundary of the IG is denoted in Fig. 8(c) by the thick red line. We note that earlier studies have referred to the Irminger Gyre as the cyclonic circulation across the full width of the Irminger Basin (e.g. Flatau et al., 2003; Lherminier et al., 2007). We strictly define the Irminger Gyre as the narrow cyclonic recirculation in the western Irminger Basin. This feature was first mapped by Lavender et al. (2000) and is displayed in Fig. 1. From the premise that the IG is a closed recirculation, the component of the WBC forming the southward limb of the gyre will be removed from our estimates of net equatorward WBC transport.

Nearly all of the hydrographic data were collected during the summer half-year period, hence our analysis is primarily representative of summertime conditions. The mean seasonal cycle from the central Irminger Sea was examined using measurements from a profiling mooring near 39°W, 59°N deployed continuously between 2003 and 2009 (F. de Jong, personal communication, 2010). At 200 m the seasonal variability in temperature was about 1.5 °C, while the salinity signal was less pronounced and only in some years reached an amplitude of 0.012. The signal decayed rapidly with depth, and vanished below about 500 m. Upper-ocean velocity measurements at the mooring site indicate a more vigorous flow field during winter, in agreement with surface

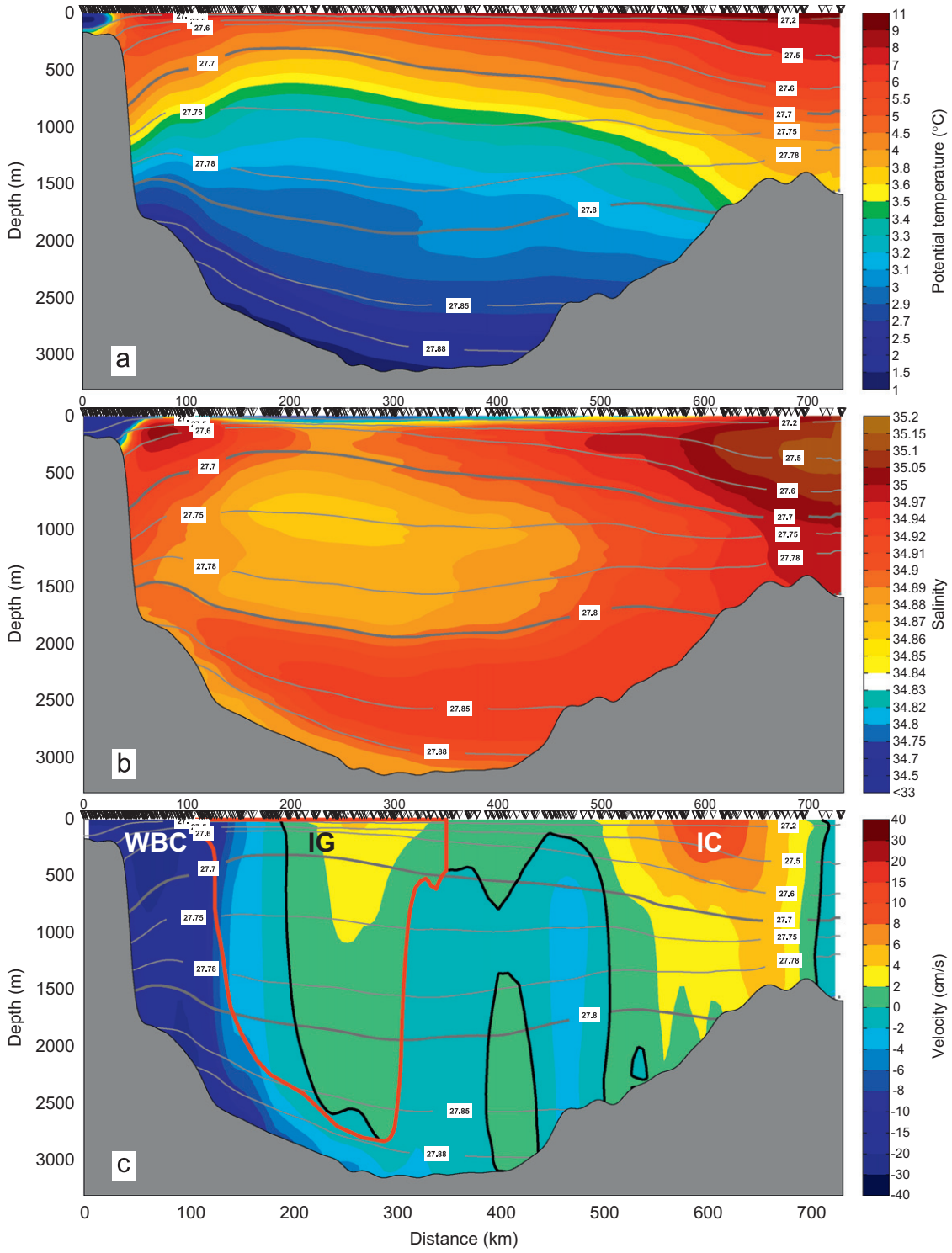

Fig. 8. Vertical sections of (a) potential temperature (°C), (b) salinity, and (c) absolute geostrophic velocity (positive to the northeast, cm/s) averaged over the period 1991–2007. The gray lines are contours of potential density, and the black and red lines in (c) are the zero velocity contour and the Irminger Gyre boundary, respectively. The black triangles indicate station locations. (For interpretation of the references to color in this figure legend, the reader is referred to the web version of this article.)

drifter data that show an enhanced wintertime circulation in the Irminger Sea (Flatau et al., 2003).

4. Temporal variability

Significant changes have taken place across the Irminger Basin in concert with the changing atmospheric conditions represented by the NAO index (Fig. 4). To document these changes we first focus on two pentads, the early 1990s (1991–1995) and the early 2000s (2001–2005), that represent distinctly different regimes of the atmospheric circulation. Following this we relate results from an EOF analysis using hydrographic, altimetric, and atmospheric reanalysis data to the NAO index and the subpolar gyre index of Häkkinen and Rhines (2004, 2009). The goal is to understand how the oceanic and atmospheric changes were interrelated.

4.1. Contrasting the early 1990s to the early 2000s

The early 1990s (1991–1995) was a period of consistently high NAO index. It was characterized by cold and stormy winters, which resulted in the formation of a large volume of LSW in the Labrador Sea (Lazier et al., 2002; Yashayaev, 2007). The resulting LSW class, the coldest and densest on record, has been referred to as lower LSW (lLSW) or $LSW_{1987–1994}$. Following this, the NAO index dropped precipitously to a strongly negative value in 1996, and the formation of lLSW ceased. In the early 2000s (2001–2005) the NAO index fluctuated between weakly positive and weakly negative values. The atmospheric forcing at the beginning of the period (winter 1999–2000) was strong enough to initiate deep convection in the Labrador Sea once again, although a less dense class of LSW was formed, called upper LSW (uLSW) or LSW_{2000} (Yashayaev, 2007; Yashayaev et al., 2007a).

To illustrate the changes that took place between these vastly different periods of atmospheric forcing, we display in Figs. 9 and 10 mean vertical sections for the early 1990s and early 2000s. The most dramatic change in the hydrography of the Irminger Sea occurred in the intermediate layer (see also Falina et al., 2007). A large pool of cold, fresh, and weakly stratified lLSW filled most of the western and central Irminger Basin between the 27.75 and 27.80 kg/m^3 isopycnals in the early 1990s. By the early 2000s the lLSW dome had essentially collapsed, and warmer, saltier, and more stratified waters occupied the basin. As the formation of lLSW ceased in the mid-1990s, the water mass became permanently isolated from the surface. Mixing with warmer and saltier waters along the margins of the basin eroded the salinity minimum and led to restratification and flattening of the isopycnals (e.g. Lazier et al., 2002). In the early 2000s there was still a trace of lLSW identifiable by the deep salinity minimum below the 27.78 kg/m^3 isopycnal. The shallower salinity minimum above the 27.75 kg/m^3 isopycnal during this period is associated with uLSW. These large-scale changes in the lower and upper LSW volumes throughout the subpolar gyre are readily detectable in chlorofluorocarbon inventories (e.g. Kieke et al., 2007). The local salinity maximum separating the two LSW modes is referred to as Icelandic Slope Water (Holliday et al., 2009). The weak stratification in the vicinity of the Reykjanes Ridge is also a signature of this intermediate water mass (Read, 2001), and is not related to LSW. The importance of local formation of LSW in the Irminger Sea versus import from the Labrador Sea will be discussed in Section 6. Warming and salinification took place in the deep layer as well, as has been quantified by previous authors (Sarafanov et al., 2007, 2010b; Yashayaev et al., 2007a,b).

The declining buoyancy forcing and collapse of the lLSW dome during the late 1990s resulted in an increase in sea surface height in the subpolar North Atlantic and a spin-down of the subpolar gyre (Häkkinen and Rhines, 2004). This is reflected in the changing structure of the boundary currents along the margins of the Irminger Sea (Fig. 10). In particular, the shallow part of the IC

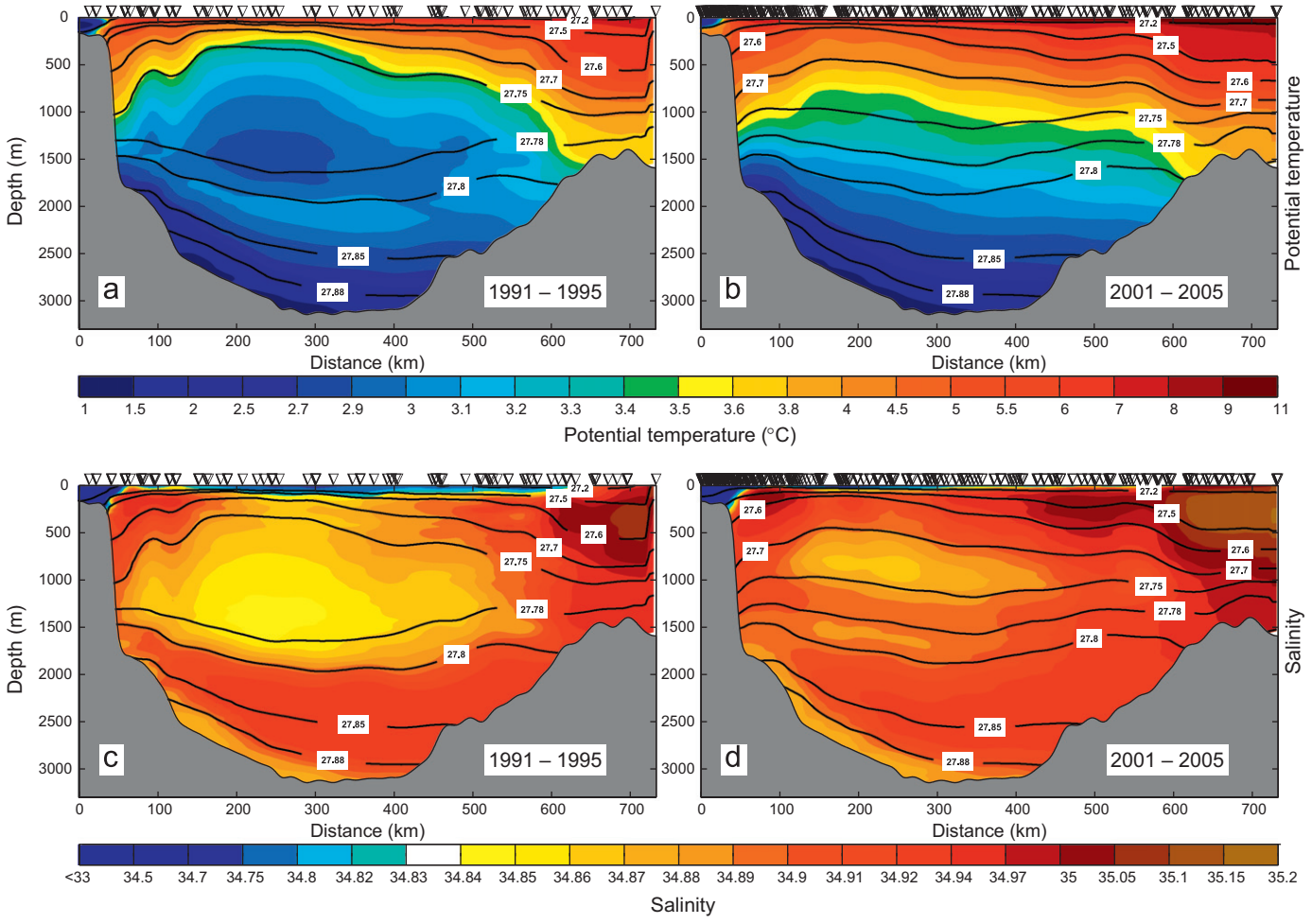

Fig. 9. Vertical sections of (a,b) potential temperature (°C) and (c,d) salinity averaged over the periods (a,c) 1991–1995 and (b,d) 2001–2005. The black contours are potential density, and the black triangles indicate station locations. (For interpretation of the references to color in this figure legend, the reader is referred to the web version of this article.)

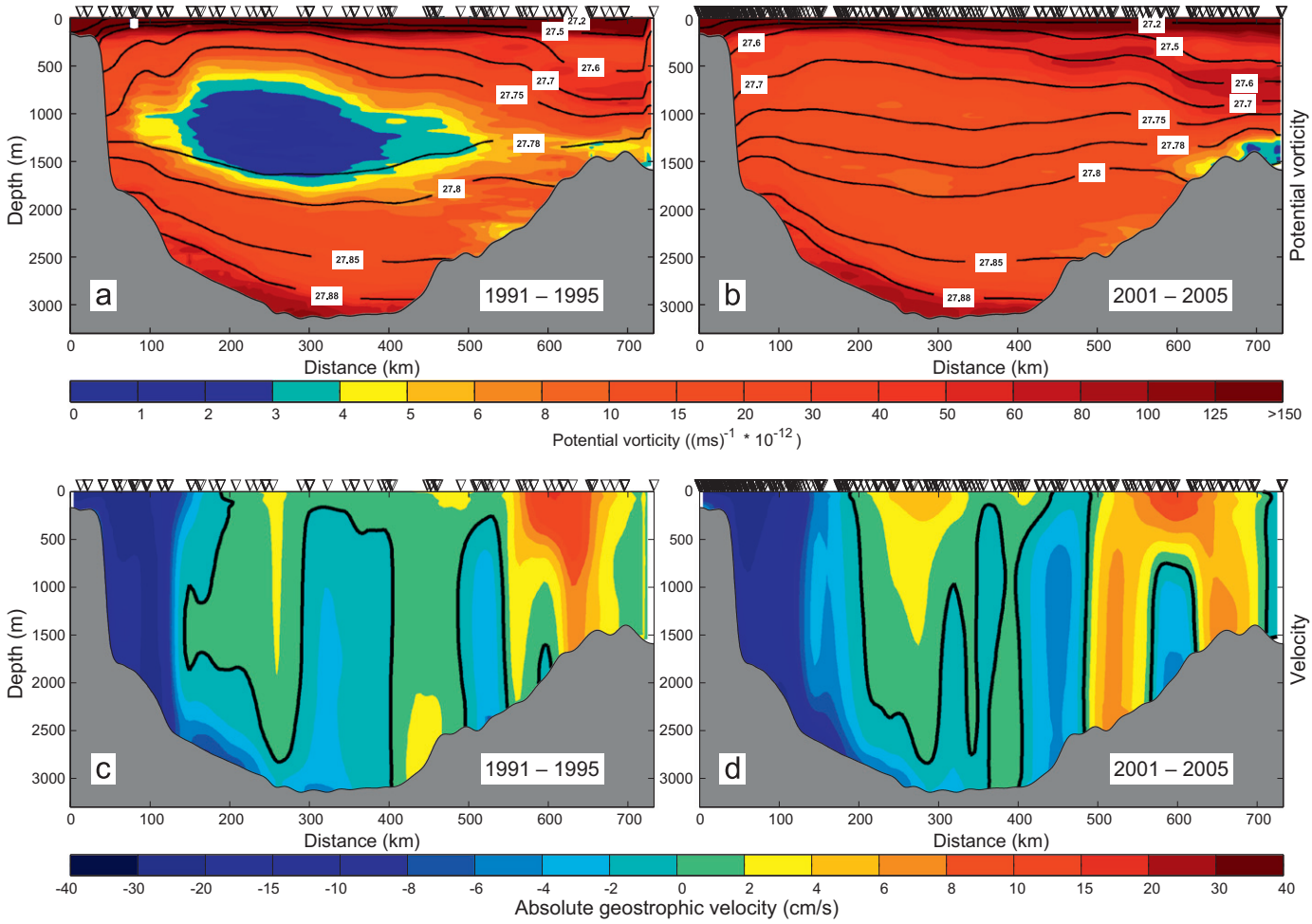

Fig. 10. As in Fig. 9, but for (a,b) potential vorticity ((ms)$^{-1}$ × 10^{-12}) and (c,d) absolute geostrophic velocity (cm/s). (For interpretation of the references to color in this figure legend, the reader is referred to the web version of this article.)

weakened between the early 1990s and the early 2000s. However, a notable change occurred in the deep structure of the IC as well. During the latter pentad a second deep extension of the current developed, centered on the 2500 m isobath (there is a weak signature of this feature during the first pentad). The influence of this varying IC structure on the transport of the current will be quantified in Section 5, and possible reasons for the structural change will be discussed in Section 7. The magnitude of the WBC also declined between the early 1990s and the early 2000s, especially in the shallow layer, consistent with the notion of a declining subpolar gyre. In contrast, the strength of the IG (located between approximately 150 and 350 km along AR7E) increased over this time period. This is surprising because both the wind stress and buoyancy components of the atmospheric forcing were significantly reduced during the latter pentad (Fig. 11), and local wind stress curl and air-sea buoyancy exchange are thought to be the main forcing mechanisms of the IG (Spall and Pickart, 2003; Pickart et al., 2003a).

Examination of the AVISO DOT field (Fig. 12a and b) provides an indication of what might have taken place. In agreement with the observations of Häkkinen and Rhines (2004) an increase in SSH is evident across the Irminger Sea (Fig. 12a and b). Closer scrutiny reveals, however, that the increase was not uniform. The extent of sea level rebound was greater in the eastern half of the Irminger Basin than in the western. As a result, the SSH gradient in the central Irminger Sea steepened. This effect is particularly evident when examining the DOT along AR7E in Fig. 13. Consequently, the northward flow of the IG, which is largely barotropic, increased. This is consistent as well with the AVISO surface geostrophic velocity field (Fig. 12c and d), where enhanced northward velocities across AR7E in the region of the IG are evident in 2001–2005 relative to 1992–1995. The velocity difference field (not shown) reveals increased velocities in most of the interior Irminger Sea north of AR7E. Increased surface flow is also evident along parts of the IC (although not at the AR7E line as discussed above), which is surprising given the general decline of the subpolar gyre circulation. The apparent paradox of a strengthening IG circulation under weakening atmospheric forcing is discussed further in Section 7.

4.2. Decadal variability

Häkkinen and Rhines (2004) used empirical orthogonal functions (EOFs) to study interannual North Atlantic sea level anomalies. Interestingly, the subpolar gyre center of action in the spatial pattern of their leading EOF mode is situated in the Irminger Sea. Häkkinen and Rhines (2004) speculate that this may be a reflection of changes in local convective activity. Too much emphasis should perhaps not be placed on the exact location of the center of action considering the small amount of variance in the altimeter data set explained by their leading mode (11%) and the southern Irminger Sea's close proximity to the geographical center of the subpolar gyre.

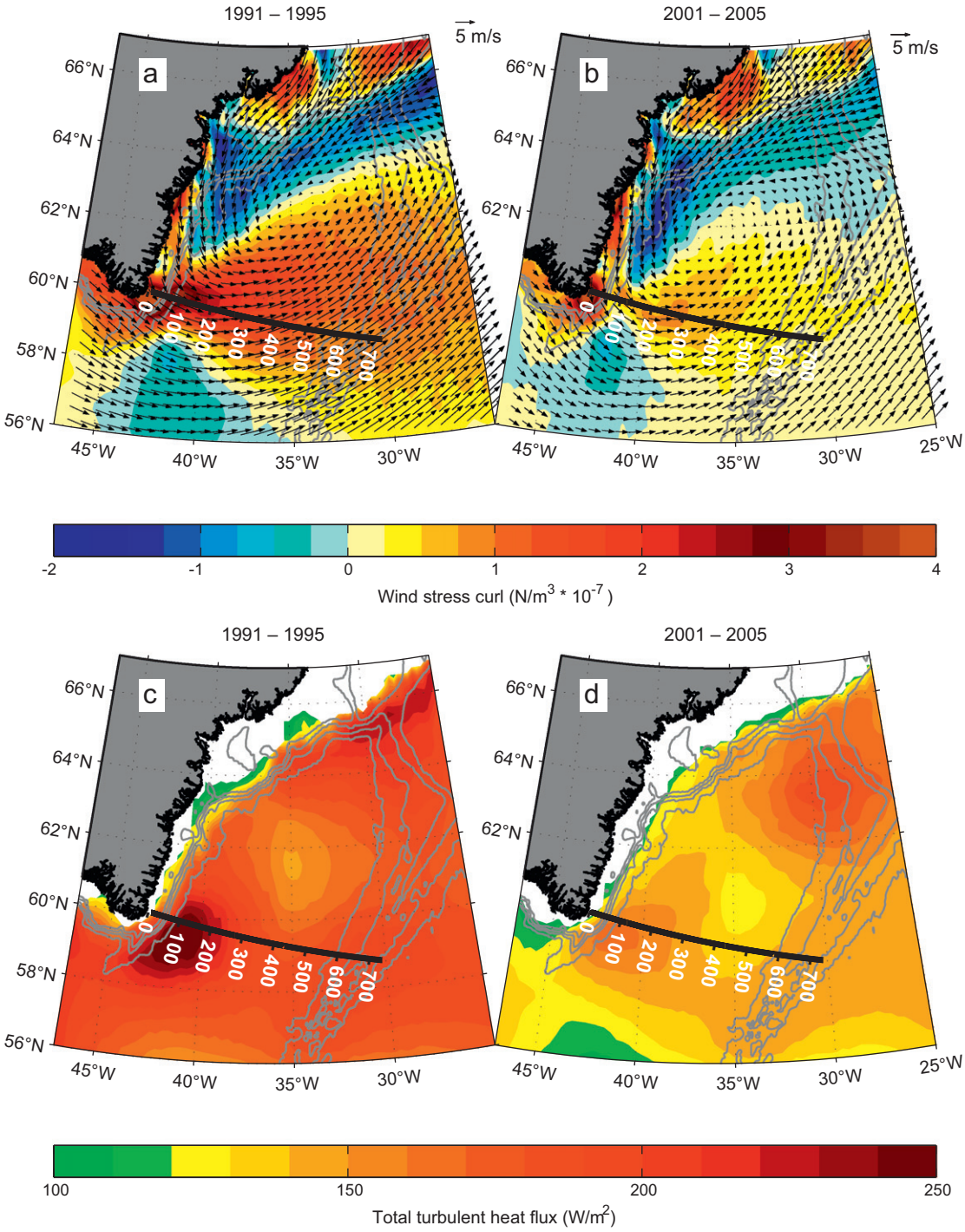

Fig. 11. Maps of NARR winter (a,b) wind stress curl ($N/m^3 \times 10^{-7}$) and wind vectors (m/s) and (c,d) total turbulent heat flux (W/m^2) averaged over the periods (a, c) 1991–1995 and (b, d) 2001–2005. The black line and numbers indicate the AR7E line and distance (in km), depth is contoured with 500 m increments starting at 500 m. (For interpretation of the references to color in this figure legend, the reader is referred to the web version of this article.)

We investigated the decadal variability with a more regional focus, and performed an EOF analysis using a wider variety of oceanic and atmospheric data from the Irminger Sea. In particular, we computed EOFs using the AR7E hydrographic data, altimetric data, and NARR atmospheric data. We performed both individual and coupled EOFs, including one calculation with all of the fields. The leading modes of all of the calculations are similar in character and represent the major evolution that took place between the early 1990s and the early 2000s. We present only the principal component (PC) timeseries and not the spatial patterns, which are similar to the pentadal averages displayed above (Figs. 9–12).

For the hydrographic EOF we used as input the annually-averaged potential temperature, salinity, and potential vorticity from the intermediate layer in the IG region to emphasize the LSW. The resulting PC timeseries explains 39% of the variance and is denoted by the black crosses in Fig. 14(a). The other timeseries in the figure are the NAO index (blue line) and the subpolar gyre index (the PC timeseries from Häkkinen and Rhines, 2004, 2009,

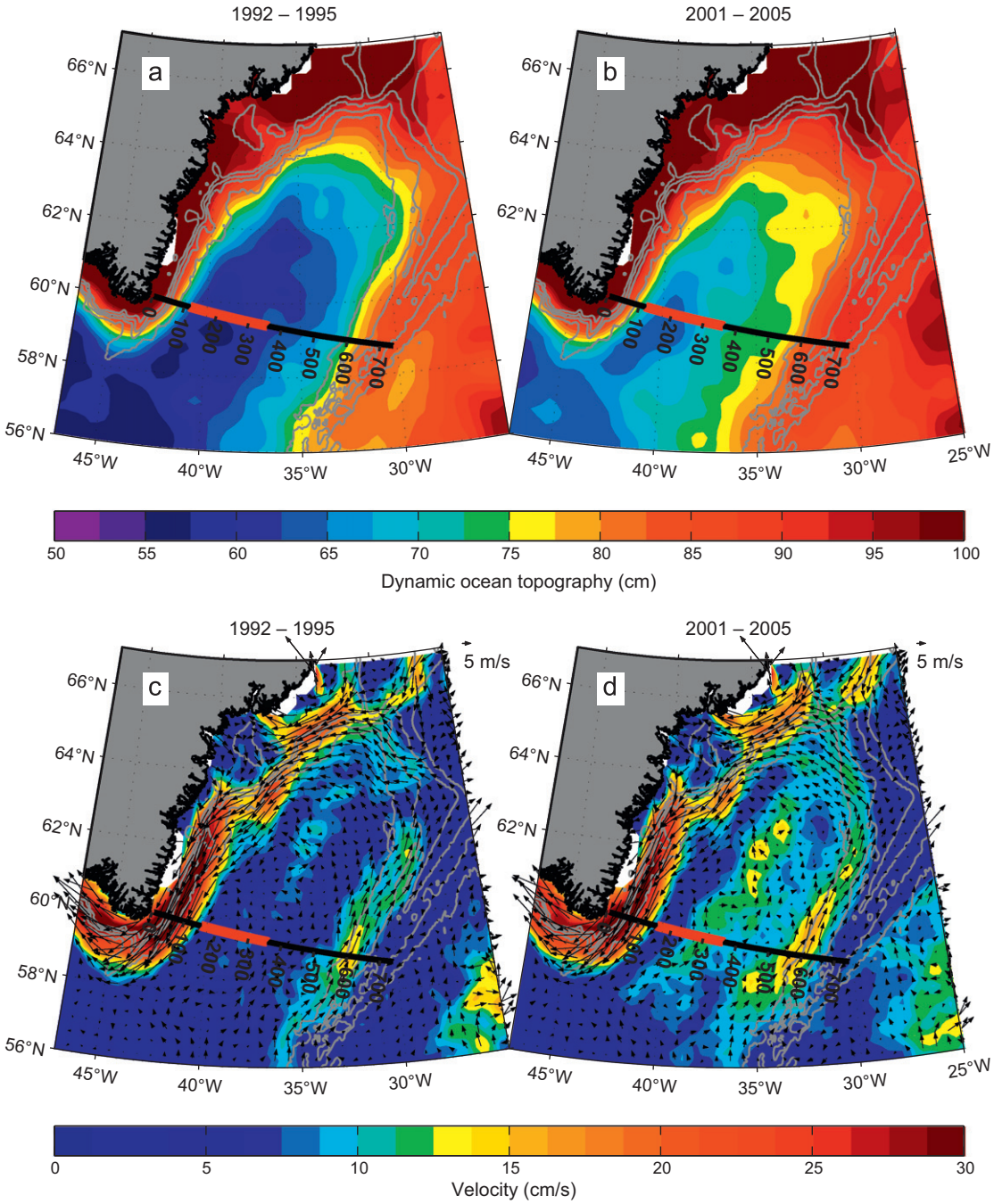

Fig. 12. As Fig. 11, but for AVISO summer absolute (a,b) dynamic ocean topography (cm) and (c,d) surface geostrophic velocity (cm/s). The red segment along AR7E indicates the width of the IG. (For interpretation of the references to color in this figure legend, the reader is referred to the web version of this article.)

red line). Note the high level of agreement between our PC timeseries and the gyre index. It is rather remarkable that the evolution of the subpolar gyre index, which represents the large-scale circulation in the North Atlantic, so closely follows the variability of the Irminger Gyre hydrography as seen in the AR7E sections. The only difference is that the gyre index peaked in early 1994, while the PC timeseries peaked around 1995. With the exception of the absolute geostrophic velocity field, which as discussed above behaved contrary to expectations in terms of the IG circulation, various other combinations of hydrographic data produce similar results. Expanding the domain from the intermediate layer in the IG to the full width and depth of the Irminger Sea led to a marginal increase in coherence with the gyre index, but a significant decrease in amount of variance accounted for. Since only 70% of the sections extended across the entire Irminger Basin, fewer data points were available from the full domain.

Next we considered an altimetric EOF using the summer mean DOT and surface geostrophic velocity fields. The resulting PC timeseries (Fig. 14(b)) explains 28% of the variance. Although the EOF is computed from a limited domain (the Irminger Sea seaward of the 1000 m isobath, north of 57°N, and between 45°W and the Reykjanes Ridge), the input data express essentially the same signal as the sea level anomalies used by Häkkinen and Rhines (2004, 2009), and the good agreement between the PC timeseries and the gyre index is not surprising. The coherence is

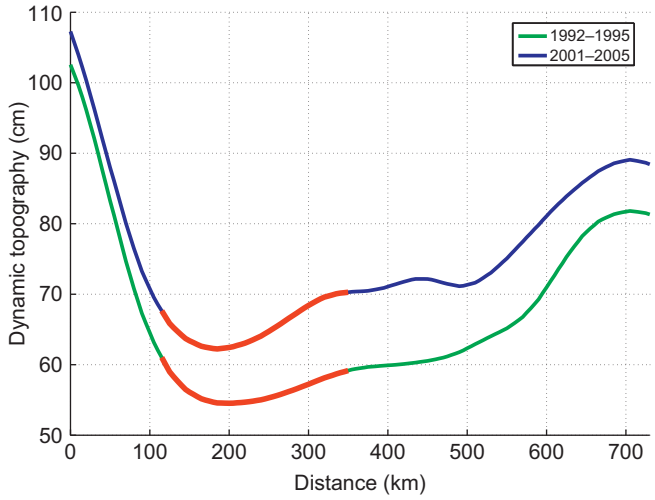

Fig. 13. AVISO DOT (cm) along AR7E for the early 1990s and the early 2000s. The width of the IG is indicated by the red segment. (For interpretation of the references to color in this figure legend, the reader is referred to the web version of this article.)

greater still when considering only the velocity field, while most variance is explained by the DOT EOF mode.

The leading atmospheric EOF mode of winter mean turbulent heat fluxes and wind stress curl from the NARR atmospheric reanalysis project (same domain as above) explains 29% of the variance in the data set. The resulting PC timeseries (Fig. 14(c)) shows some degree of coherence with the NAO index (correlation of 0.70, significant at the 99% confidence level), which indicates that the NAO index is useful as a representation of the wintertime atmospheric forcing in this region over the time period considered. The strongest signal is found directly east of Cape Farewell (Fig. 11), which reflects the importance of the tip jet in this region (e.g. Pickart et al., 2003a). As noted above there is also a positive correlation between the NAO index and the number of tip jet events per winter. The atmospheric variability represented by the NAO index influences a region that extends well beyond the Irminger Sea. Even though the NAO index displays a substantial amount of short-term fluctuations, the spin-down and contraction of the subpolar gyre is possibly a reflection of the long-term decline in the NAO index from its the maximum in the early 1990s (see for example Sarafanov, 2009, Fig. 1(d)). This is not very obvious from the temporally limited PC timeseries in Fig. 14, but it should not be surprising that the ocean and the atmosphere operate on different time scales.

5. Transports

Transports of the three primary features of interest – the Irminger Gyre, the Irminger Current, and the Western Boundary Current – have been estimated using the annually-averaged absolute geostrophic velocity sections described above. In the following figures (Figs. 15–18) the black error bars represent the full uncertainty. This is a combination of the geoid error estimate, the AVISO reference velocity standard error, and the statistical error resulting from usage of a small number of synoptic density sections in the annually-averaged density fields, which are the three dominant error terms (see the appendix). The geoid error is constant in time,[3] while the magnitude of the statistical error depends on the number of sections per year. The blue error bars represent only the AVISO standard error, which does vary from year to year, and hence is the only dominant error term that will directly impact the trend. The reader should keep in mind the extrapolation used to produce absolute geostrophic velocity sections for 1991 and 1992, and hence the increased uncertainty of the transports in those years.

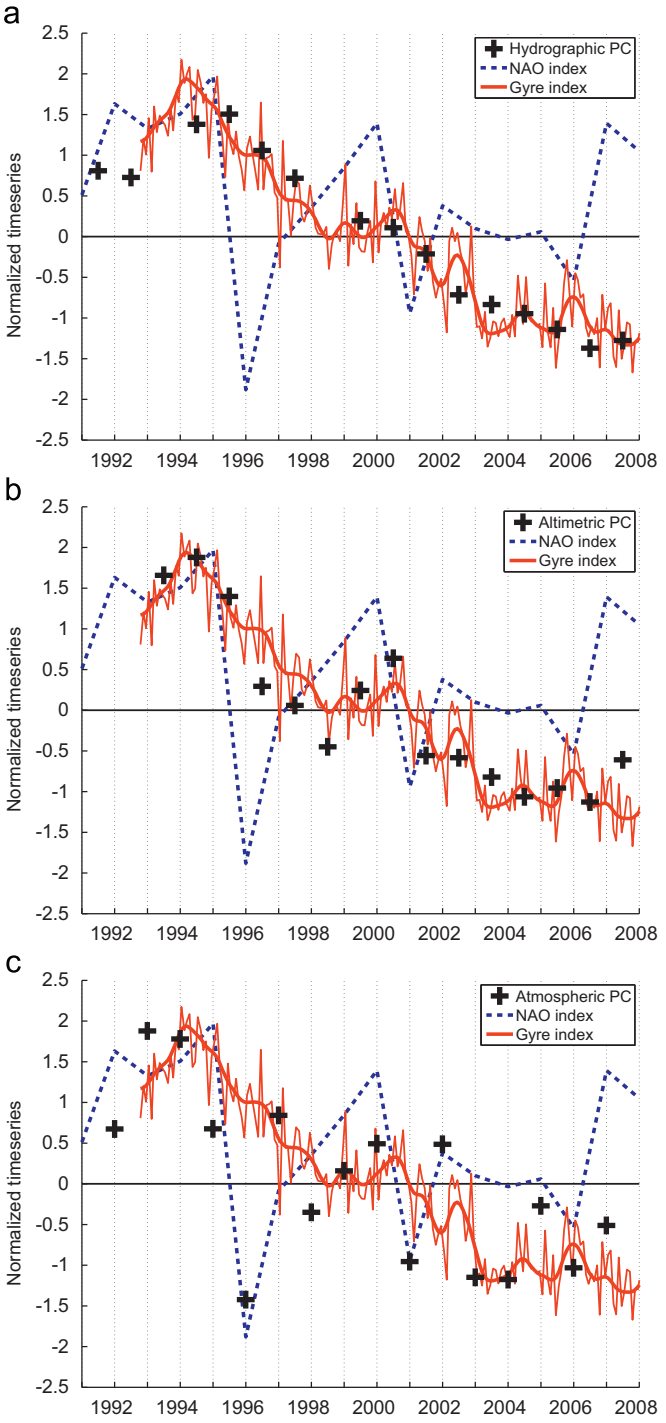

Fig. 14. Principal component (PC) timeseries of the first EOF mode computed from (a) annual mean hydrographic data (potential temperature, salinity, and potential vorticity), (b) summer mean altimeter data (dynamic ocean topography and surface geostrophic velocity), and (c) winter mean atmospheric reanalysis data (turbulent heat fluxes and wind stress curl). The blue and red timeseries are the NAO index and the gyre index of Häkkinen and Rhines (2004, 2009), respectively. (For interpretation of the references to color in this figure legend, the reader is referred to the web version of this article.)

[3] The geoid error will appear to have temporal variability as the width of the feature under consideration was not constant; for the same transport a broad and sluggish current will have a greater uncertainty than a narrow and swift current.

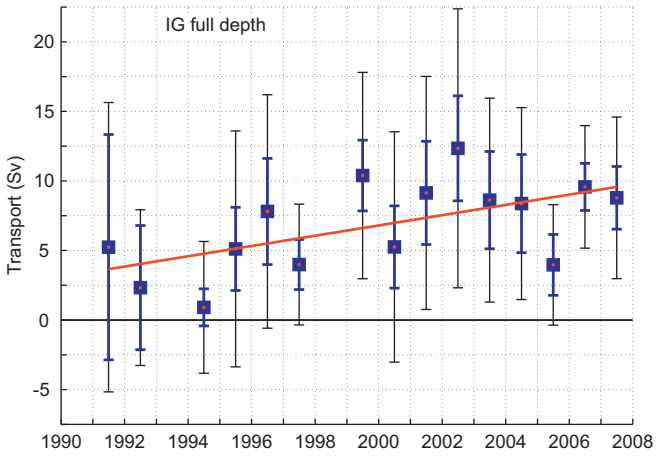

Fig. 15. Irminger Gyre transport in Sv. The black error bars indicate the total error, while the blue error bars show the AVISO standard error only. The red line is the least squares best fit through the data. (For interpretation of the references to color in this figure legend, the reader is referred to the web version of this article.)

5.1. The Irminger Gyre

The IG was typically located between 150 and 350 km along the AR7E line (Fig. 8(c)). Although it was present every summer, there was considerable interannual variability in terms of its width and magnitude. The transport was estimated from the northeastward flow to the east of the gyre center (assuming an equal return flow in the WBC). The resulting transport timeseries of the IG is presented in Fig. 15. As noted earlier in Section 4, the magnitude of the gyre circulation increased through the observational period, which is supported by the trend of increasing transport at a rate of 3.7 Sv per decade. The trend was found to be significantly different from zero at a confidence level of 95% using the reverse arrangements test of Bendat and Piersol (1986). Rather than assuming a linear trend, the transport time series may instead be considered to represent two distinct states; first a weaker phase up to 1998 followed by a more vigorous phase after 1998. The null-hypothesis, that the transports before and after 1998 had the same median value, was evaluated using the Wilcoxon rank sum test (Wilcoxon, 1945), and had to be rejected at the 99% confidence interval. The IG clearly spun up during the period of observations; whether the change was gradual or took place more abruptly around 1998 is difficult to assess considering the high uncertainty in our annual transport estimates.

The mean IG transport over the full 17-year period was 6.8 ± 1.9 Sv. An alternative way to compute the mean transport of the IG is directly from the mean absolute geostrophic velocity (Fig. 8(c)) instead of from the transport timeseries. The resulting mean transport estimate is lower, only 4.2 ± 1.9 Sv. This discrepancy exists because the location of the gyre changes from year to year as well as its strength. Hence the average of the individual timeseries values can be thought of as a "stream coordinate" mean.

5.2. The Irminger Current

The IC is steered by the topography of the Reykjanes Ridge, and was typically found between 500 and 700 km along AR7E (Fig. 8(c)). The full-depth IC transport timeseries is displayed in Fig. 16(a). Surprisingly, we found a weak trend of increasing IC transport, which is contrary to the notion of a declining subpolar gyre circulation. There is, however, considerable interannual variability, and the 1.9 Sv per decade trend is not significantly different from zero. Removal of the high-uncertainty transport estimates from 1991 and 1992 referenced by extrapolated surface velocities does little to improve the significance of the trend. Closer inspection reveals that the positive trend is caused by a transport increase at depth. In fact, the transport in the upper 500 m decreased into the 2000s (Fig. 16(b)), consistent with the conclusions of Häkkinen and Rhines (2004, 2009). The deep transport increase in the IC (Fig. 16(c)) is largely the result of the emergence of the second deep extension of the IC noted

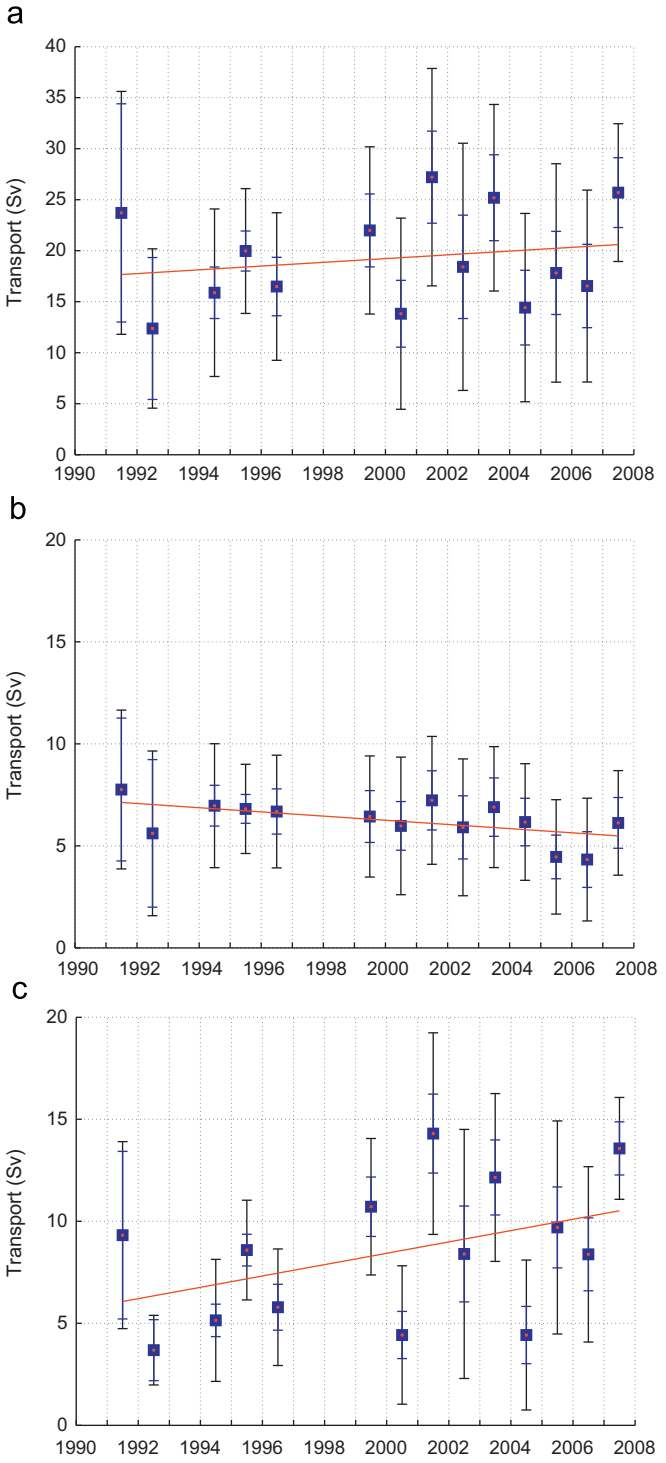

Fig. 16. As Fig. 15, but for the Irminger Current. (a) Full IC transport, (b) IC transport above 500 m, and (c) IC transport below 1000 m. Note the different vertical scale in (b) and (c).

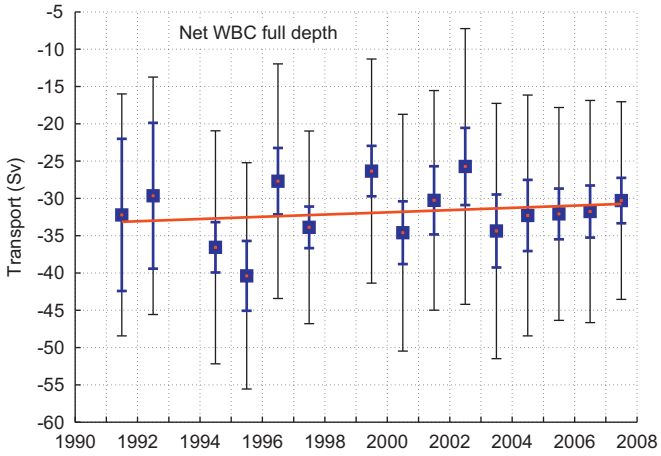

Fig. 17. As Fig. 15, but showing net Western Boundary Current transport.

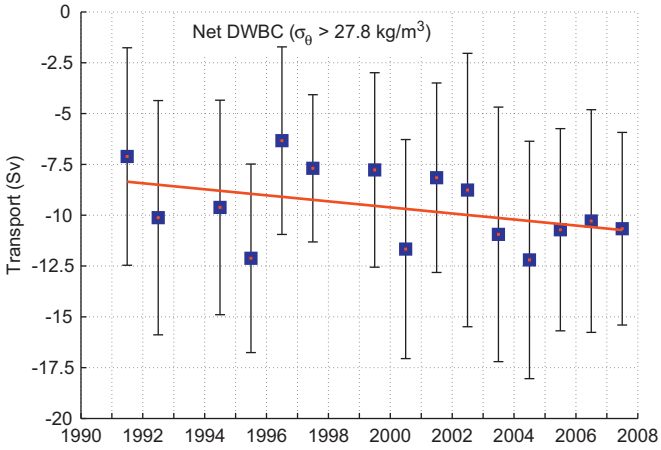

Fig. 18. As Fig. 15, but showing net Deep Western Boundary Current transport. For the DWBC the total error (black error bars) includes an estimate of the bottom triangle error.

in Section 4. The changing structure of the deep IC will be discussed more extensively in Section 7, including the possible causes.

The mean of the full-depth IC transport timeseries was 19 ± 3 Sv. For comparison with previous estimates we also computed the transport of waters less dense than $\sigma_\theta = 27.76$ kg/m^3 whose average value was 12 ± 2 Sv. The corresponding synoptic transport reported by Pickart et al. (2005)[4] for their August 2001 occupation was 13.7 Sv. While this is a bit larger than our average value, it compares well with our 2001 estimate of 14 ± 6 Sv. IC transports were also provided by Bacon (1997): 9 Sv ($\sigma_2 < 36.873$ kg/m^3 in 1991) and Lherminier et al. (2010): 11 ± 2 Sv ($\sigma_2 < 36.94$ kg/m^3 in both 2002 and 2004). The IC transport computed directly from the mean vertical section of absolute geostrophic velocity (Fig. 8(c)) is 13 ± 3 Sv. As was the case for the IG transports, this value is reduced compared to the temporal average of the discrete estimates presented above. In the IC case, however, meandering of the current is not the cause of this reduction; rather, it is due primarily to the significant changes in the current's deep structure.

[4] Pickart et al. (2005) also provides a list of previous, unreferenced IC transport estimates, none of which exceed 10 Sv.

5.3. The Western Boundary Current system

We consider the Western Boundary Current (WBC) to be the southward flow bounded by the Greenland shelfbreak to the west (30 km along AR7E) and the deepest part of the Irminger Gyre in the east (typically located around 280 km, see Fig. 8(c)). The bottom of the Irminger Gyre (sometimes it extended all the way to the sea floor) is close to the deepest point of the Irminger Basin, and thus our definition of the WBC is in general agreement with that of Holliday et al. (2009), although they also included the outer part of the Greenland shelf in their calculations. In 1995 the section did not extend farther onshore than to 50 km. To compensate for the missing part of the WBC transport that year, the mean transport between 30 and 50 km (-3.2 Sv) was added to the 1995 estimate, and the error was increased by the standard deviation of the mean transport within the given interval. As the DWBC does not extend inshore of 50 km, it is not affected by the modification to the 1995 velocity section.

Traditionally, all of the southward flow on the western side of the Irminger Basin is taken into account in estimates of WBC transport. For comparison with previous results we have computed WBC transports in the same fashion, hereafter called the southward WBC transport. We do, however, emphasize timeseries of WBC transport with the IG return flow removed under the premise of a closed IG recirculation—which is referred to as the net WBC transport. The net WBC transport is the throughput of the boundary current system, hence it is the more appropriate quantity to consider when discussing the Meridional Overturning Circulation.

The net surface to bottom WBC average transport (Fig. 17) was -32 ± 4 Sv (keep in mind that southward transports are negative). There is a slight indication of weakening of the WBC, but the trend is not significant. The range of interannual variability was 15 Sv. When considering the southward WBC transport, the average transport is larger, -39 ± 4 Sv. Interestingly, there was a significant trend of increasing southward WBC transport of -2.2 Sv per decade. However, this is predominantly because the Irminger Gyre spun up over this time period (by 3.7 Sv per decade, see above). In the case of the WBC there was good agreement between the mean transport computed from the transport timeseries and from the mean vertical section of absolute geostrophic velocity (-38 ± 3 Sv, Fig. 8(c)). This was expected given the lack of WBC spatial variability, unlike the IG and IC cases above.

Earlier surface to bottom WBC estimates from the southern Irminger Sea and Cape Farewell region include: -33.5 Sv (synoptic section referenced by 2-month current meter records from 1978, Clarke, 1984), -32.2 and -40.5 ± 8.1 Sv (ADCP-referenced synoptic sections from 1991 and 2005, respectively, Bersch, 1995; Holliday et al., 2009), -26.5 Sv (inverse model constrained by ADCP data from 1991, Bacon, 1997), and -39.0 ± 1.8, -29.5 ± 2.1, and -34.9 ± 2.5 Sv (also an inverse model constrained by ADCP data, from 1997, 2002, and 2004, respectively, Lherminier et al., 2007, 2010). Our southward WBC transport of -39 ± 4 Sv is in the upper range of the previous transport estimates. Fig. 6(a) shows that the AVISO velocities are greater than the ADCP-referenced velocities in this region by approximately 2 cm/s, predominantly in the western part of the WBC. An attempt to correct for this possible AVISO bias near the Greenland coast using the ADCP-referenced velocities results in a reduction of the southward WBC transport by approximately 3 Sv. However, the error associated with the ADCP-referenced velocities is large enough that such a correction is not justified.

5.4. The Deep Western Boundary Current

Given its importance to the Meridional Overturning Circulation, we also considered the DWBC component ($\sigma_\theta > 27.80$ kg/m^3) of the

WBC, which is composed of DSOW and ISOW (see the appendix for a discussion of the bottom triangle errors). As in the case of the WBC we emphasize net transports (although for the DSOW layer, into which the IG only sporadically reached, the difference between southward and net transports is minimal). The net DWBC average transport (Fig. 18) was -9.6 ± 1.4 Sv. This can be split into -7.3 ± 1.0 Sv and -2.4 ± 0.5 Sv for the ISOW and DSOW components, respectively. During the 17-year observational period the net DWBC transport increased at a rate of -1.5 Sv per decade (the trend was significant at the 95% confidence level). The increase in DWBC transport is consistent with results from earlier studies. Using a reference level at 1000 m, Sarafanov et al. (2009) found a similar significant trend of increasing baroclinic transport over the same time period. Combining altimetry-derived surface velocities and baroclinic velocities from hydrographic data, Sarafanov et al. (2010a) determined that the absolute DWBC transport increased as well between the mid-1990s and the 2000s. A trend of increasing DWBC transport was also found in the Labrador Sea from the late 1990s to the early 2000s (Dengler et al., 2006). Extending their timeseries using equivalently computed baroclinic transports from Bacon (1998), Sarafanov et al. (2010a) detected a robust negative correlation between DWBC transport anomalies and Labrador Sea LSW thickness anomalies, such that enhanced DWBC transport is associated with decreasing LSW thickness. This relationship was found farther south (west of the Grand Banks of Newfoundland) as well by Pickart et al. (1999).

For the full southward DWBC we obtain a mean transport of -11.3 ± 1.3 Sv (with a trend of -2.9 Sv per decade significant at the 99% confidence level—consistent in sign and magnitude with the results of Sarafanov et al. (2010a), who inferred that the DWBC transport increase between the mid-1990s and 2000s was more than 2 Sv at the 86% confidence level). This estimate is in the upper range of absolute DWBC transport measurements of -7.3 to -12.3 Sv made within the last two decades for the southern Irminger Sea and Cape Farewell region (e.g. Bersch, 1995; Lherminier et al., 2007, 2010; Holliday et al., 2009; Bacon and Saunders, 2010). As discussed by Bacon and Saunders (2010) there is considerable variability in the DWBC transport record on a variety of temporal scales. The interannual variability of our timeseries spans the range of previously measured transports. The possible AVISO bias discussed above would result in a similar overestimate of our DWBC transport as well. In agreement with Bacon and Saunders (2010), our results imply then that the mean DWBC transport in the vicinity of Cape Farewell is at least 2 Sv smaller than the commonly quoted value of 13.3 Sv (Clarke, 1984).

6. Convection

The paradigm describing the LSW formation process proposed by McCartney and Talley (1982) and recently updated by Brambilla and Talley (2008) contends that LSW is the end-product of "subpolar mode waters" that are continuously densified via air-sea interaction within the cyclonic flow around the subpolar gyre. This culminates with deep convection in the Labrador Basin, forming the weakly stratified LSW. In contrast, a growing body of evidence suggests that deep convection also takes place in the Irminger Sea during severe winters, leading to a second location of LSW formation (e.g. Pickart et al., 2003a,b; Bacon et al., 2003; Falina et al., 2007; Våge et al., 2008, 2009a). These studies have underscored the importance of small-scale oceanic (the Irminger Gyre) and atmospheric (the westerly Greenland tip jet) features that conspire to provide conditions favorable for deep convection in the southwestern Irminger Sea.

Despite this body of evidence, recent studies argue that the LSW signature in the Irminger Basin is principally due to advection from the Labrador Sea on the time scale of ~2 years, with little or no local convection east of Greenland. One such study (Bersch et al., 2007) presents evidence that there has been an intermediate salinity maximum layer continuously present (and intensifying) in the Irminger Sea since 1991, implying that deep overturning could not have occurred during this time period. We now examine this issue using the collection of AR7E sections, following the volumetric T-S approach of Yashayaev (2007). We find strong evidence that deep convection occurred locally in the Irminger Basin during the early 1990s. Furthermore, we identify a separate signal of remotely-formed LSW advected into the Irminger Sea from the west.

6.1. Intermediate salinity maximum layer

One of the pieces of evidence used to discount the notion of local convection in the Irminger Sea stems from the recent analysis of Bersch et al. (2007). They used time series obtained from a subset of the AR7E hydrographic sections averaged between 34 and 41°W (i.e. the full width of the deep Irminger Basin, see Fig. 3) to investigate changes in the characteristics and distribution of LSW in the Irminger Sea. Computing the temporal changes of salinity relative to 1991 (ΔS_{91}), they found a layer of positive ΔS_{91} at a density of approximately $\sigma_1=32.38$ kg/m^3 ($\sigma_{1.5}=34.655$ kg/m^3, between 600 and 1200 db) that was continuously present since 1991 (see Fig. 8(b) in Bersch et al., 2007). This layer coincides with the Icelandic Slope Water intermediate salinity maximum that separated the lower and upper LSW water masses of the 2001–2005 pentad (Fig. 9(d), see also Holliday et al., 2009). Bersch et al. (2007) interpreted this as evidence that there was no significant formation of the densest class of LSW in the Irminger Sea, even during the high-NAO period of the early 1990s. They argued that, had there been convection, fresh surface water would have penetrated the $\sigma_1=32.38$ kg/m^3 isopycnal causing an interruption of the positive ΔS_{91} layer.

It is important to note that Bersch et al. (2007) averaged properties over the entire deep Irminger Basin, from the base of the Greenland continental slope to the western flank of the Reykjanes Ridge (Fig. 3). However, if deep convection occurs in the Irminger Sea, it likely does so primarily within the southwestern portion of the basin (Pickart et al. 2003a,b; Centurioni and Gould, 2004). This region is under the direct influence of the cyclonic Irminger Gyre and the Greenland tip jet, and is the part of the Irminger Sea where the oceanic and atmospheric conditions are most favorable for deep overturning. With this in mind, we redid the calculation of Bersch et al. (2007) using hydrographic data confined to the location of the IG along AR7E (150–350 km, see Fig. 8(c); the results are not very sensitive to the exact limits).

A contrasting result from Bersch et al. (2007) is obtained when the data are confined geographically as such. Fig. 19(a) shows the temporal evolution of salinity and potential density. In agreement with Bersch et al. (2007), the peak of the LSW dome occurred in 1995. By 2001 it had collapsed (see also Fig. 9(d)). However, when considering only the western portion of the Irminger Basin within the IG, the isopycnal doming was much more pronounced (Fig. 19(a)). In particular, the $\sigma_{1.5}=34.655$ kg/m^3 contour that, according to Bersch et al. (2007), delimits the density of locally formed water masses reached a minimum pressure of less than 400 db in 1995. Keep in mind that the data used here were collected in summer. It is highly unlikely that the mixed layer depth in this region did not exceed 400 db during the winter of 1994–1995 (during the high-NAO period). This suggests strongly that the lLSW layer was locally ventilated. Mixed layers deeper than 400 db were routinely observed by profiling floats and

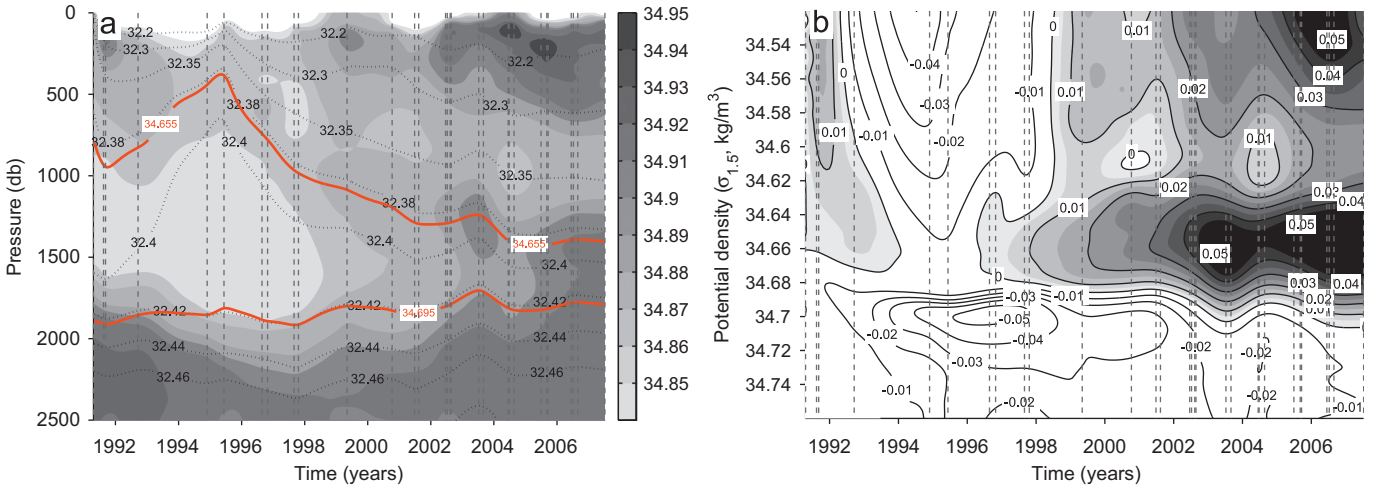

Fig. 19. Temporal changes of (a) salinity (shaded) and density (σ_1, contours): and (b) salinity relative to 1991 (positive values are shaded) on density surfaces ($\sigma_{1.5}$). The figures are based on data averaged from within the IG. The dashed lines indicate when measurements were made. The $\sigma_{1.5}$=34.655 kg/m^3 and $\sigma_{1.5}$=34.695 kg/m^3 contours are highlighted in red. (For interpretation of the references to color in this figure legend, the reader is referred to the web version of this article.)

moorings during the winters of the early 2000s, which, unlike the early 1990s, were characterized by a low NAO index and a well-stratified water column (Centurioni and Gould, 2004; Våge et al., 2008, 2009a). Furthermore, our calculation of ΔS_{91} using hydrographic data from within the IG does indeed show an interruption of the positive ΔS_{91} layer between 1994 and 1996, which again suggests that lLSW was formed during this period. The $\sigma_{1.5}=34.695$ kg/m^3 contour indicates the bottom of the lLSW layer and likely represents the absolute lower limit to convection in the Irminger Sea during this period. This calculation reinforces the arguments made to date that, under strong atmospheric forcing, deep convection can occur in the Irminger Sea. It also illustrates some of the subtleties involved in investigating convection in that basin.

6.2. Labrador Sea Water layer thickness

Encouraged by the above results showing that deep convection likely occurred in the western Irminger Sea in the early 1990s, but realizing that LSW was also likely advected from the Labrador Sea to the east, we studied in greater detail the evolution of the LSW inside and outside of the Irminger Gyre. The LSW core was identified following the volumetric density layer approach of Yashayaev (2007). The method involves calculation of the thickness of a continuum of potential density (σ_2) layers. A mean vertical density profile for each section within the chosen lateral boundaries was first determined. The vertical extent (thickness) of every layer of width $\Delta\sigma_2=0.01$ kg/m^3 was then computed. Individual layers were separated by 0.002 kg/m^3. The LSW core was then easily identified by the density layer of largest thickness. An advantage of this method is its ability to take into account changes in water mass properties since it does not rely on time-invariant hydrographic bounds to identify the water mass.

The spreading of LSW from the Labrador Sea was investigated by Pickart et al. (2003b) using the advective-diffusive model of Straneo et al. (2003), which was based on a realistic flow field determined from float measurements containing the interior recirculations in the Labrador and Irminger seas (Lavender et al., 2000). In agreement with recent observationally based estimates (e.g. Falina et al., 2007; Yashayaev et al., 2007a), the time for LSW to travel from the Labrador Basin to the central Irminger Basin was approximately 2 years. Once inside the Irminger Sea, the model tracer was observed to wrap around the Irminger Gyre (Straneo et al., 2003), taking another year to penetrate to the gyre's center (Pickart et al., 2003b). Another advective-diffusive model study indicates that the LSW distribution resulting from sources in both the Labrador and Irminger seas correspond better to observations than a single source of LSW in the Labrador Sea alone (Kvaleberg et al., 2008). The observed LSW distribution in the Irminger Sea likely results from a combination of the two LSW sources. The LSW formed in the Labrador Basin is in general colder, fresher, and denser than the LSW formed locally in the Irminger Sea (Pickart et al., 2003b). Hence we expect that the arrival of the remote LSW will present an unmistakable signal in the Irminger Sea LSW timeseries derived from the volumetric approach. Furthermore, the strongest remotely-formed LSW signal should occur outside of the gyre (i.e. to the east of the northward limb of the gyre).

As a first calculation we applied the volumetric method to the center of the Irminger Gyre, between 200 and 300 km along AR7E. These narrow bounds (on average the gyre was located between 150 and 350 km) were chosen to avoid contamination from LSW outside of the gyre, but the outcome is not very sensitive to this particular choice. The resulting average layer thickness versus time and density is shown in Fig. 20. The most notable feature is the LSW dome that reached its greatest volume in 1995 (in good agreement with Fig. 19(a) and Bersch et al., 2007). This agrees well with the modeled mixed layer depth in the winter of 1994–1995 exceeding 1700 m (Våge et al., 2008). Indeed, the bottom of the thickest 1995 σ_2 level was found at a depth of 1730 m in summer 1995 (Fig. 21(b)). In contrast, the thickest layer of the lLSW class was formed in the Labrador Sea in the winter of 1993–1994 (Yashayaev, 2007), although lLSW formation did not shut down until after the following winter (e.g. Avsic et al., 2006). Had the LSW observed inside the Irminger Gyre been ventilated remotely in the Labrador Sea, one would expect to see the thickest LSW layer at the center of the gyre at the earliest three years later, in 1997. At this time, however, the Irminger Gyre lLSW dome was already collapsing. Timeseries of lLSW core properties within the Irminger Gyre are shown in Fig. 21. One sees a single extremum in the layer thickness, salinity, and temperature. (We note that even though the layer thickness started declining immediately in 1996, the temperature and salinity remained low for one more year, perhaps due to some amount of remotely-formed LSW penetrating the gyre.)

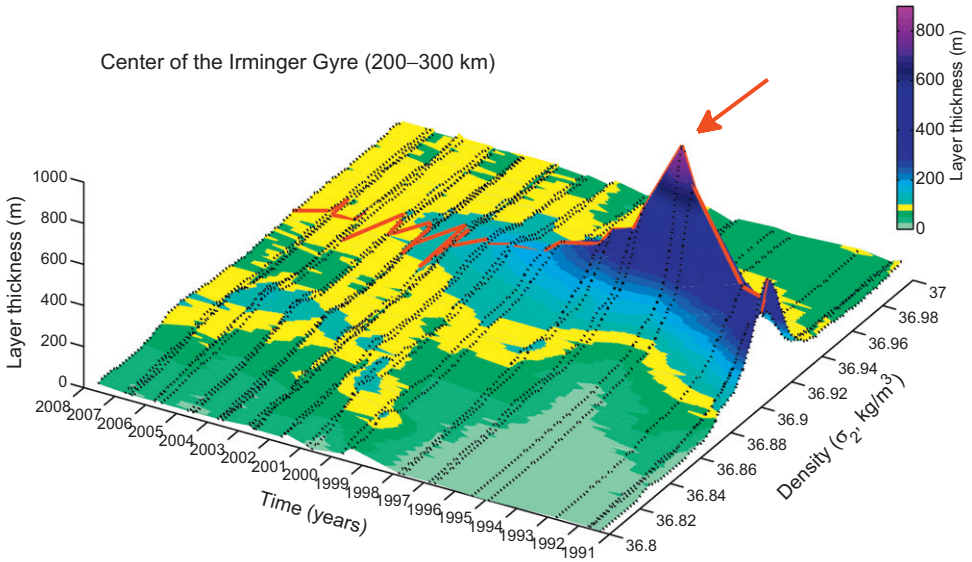

Fig. 20. Average thickness (in m) of potential density layers within the Irminger Gyre (200–300 km along AR7E) in relation to potential density (σ_2, kg/m^3) of the given layer and time (years). The vertical extent of each overlapping layer was 0.01 kg/m^3, and individual layers were separated by 0.002 kg/m^3. The red line follows the crest of the thickness ridge and hence identifies the lLSW core in each section, and the red arrow identifies the lLSW peak. The dashed lines indicate when individual sections were occupied. (For interpretation of the references to color in this figure legend, the reader is referred to the web version of this article.)

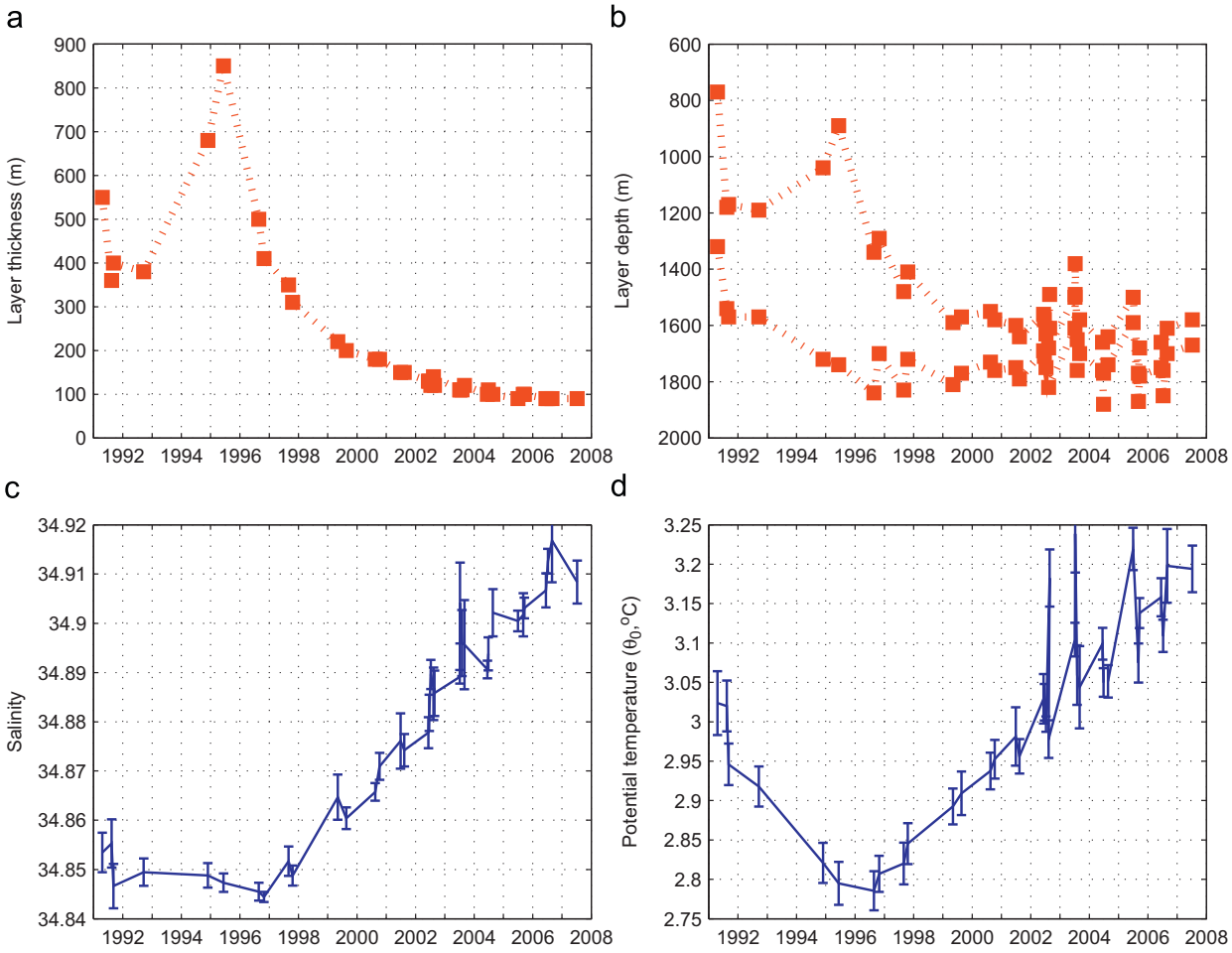

Fig. 21. Timeseries of core lLSW properties. (a) Layer thickness (m). (b) Upper and lower bounds of the layer in (a). (c) Salinity. (d) Potential temperature (°C). One standard deviation is indicated by the error bars.

Note also the arrival of the shallower LSW mode around 2000 (at a density of approximately 36.84 kg/m^3 in Fig. 20). While not as prominent as in the Labrador Sea (see Fig. 6(a) in Yashayaev, 2007), some uLSW evidently formed within the Irminger Gyre as well. The thickness of the uLSW layer appears to have increased noticeably between 2004 and 2005, perhaps due to arrival of uLSW from the Labrador Sea.

Now we contrast the results of the volumetric density layer calculation within the Irminger Gyre to that outside of the gyre. Fig. 22 corresponds to Fig. 20, but is constructed using data from the eastern part of the Irminger Basin, between 400 and 500 km along AR7E. The bounds were chosen such that the domain was well outside the Irminger Gyre while still to the west of the Irminger Current. The difference between the two figures is striking. The lLSW dome is much smaller in magnitude (the maximum lLSW thickness was about 500 m compared to more than 800 m inside the gyre), but now there is a second peak in 1997. This is seen more clearly in the timeseries of layer thickness, salinity, and temperature outside of the gyre (Fig. 23). In contrast to the center of the gyre, there are now two extrema in these properties. The timing of the second peak (1997) is consistent with a 2–3 year time lag from the Labrador Sea. Furthermore, the second peak is colder, fresher, and deeper, consistent with the more extreme properties of the LSW formed in the Labrador Basin. Finally, the mean absolute velocity section for the pentad of the early 1990s (Fig. 10(c)) shows northeastward flow in the region outside of the gyre (between 400 and 500 km), consistent with a remote pathway from the Labrador Sea. We note that the earlier LSW peak implies some degree of local convection outside of the gyre, which was observed in winter 2007–2008 (de Jong, 2010).

To summarize, we have demonstrated that inside of the Irminger Gyre there was an interruption of the intensifying intermediate salinity maximum layer that purportedly placed a limit to the depth of local convection in the early 1990s. Indeed, examination of the LSW layer thickness evolution shows a single peak of lLSW in 1995, too early to be a remote signal from the maximum convection year in the Labrador Sea (1994). However, outside of the gyre there were two maxima. The timing and properties of the latter peak are only explainable by a remote Labrador Sea source, consistent as well with the velocity field.

7. Discussion

Our results indicate that the Irminger Gyre circulation intensified between the early 1990s and the early 2000s, with the transport increasing at a rate of 3.7 Sv per decade. This was unexpected given the general decline in atmospheric forcing that occurred through the period of observations. Inspection of the AVISO dynamic ocean topography field revealed that the general increase in SSH across the entire subpolar gyre was not uniform within the Irminger Sea, but that the eastern half of the basin rebounded to a greater degree than the western, leading to a steeper gradient across the IG and hence the stronger circulation (Fig. 13). Analysis of the AR7E hydrographic data indicate that part of the SSH change was due to steric height differences. In particular, from the early 1990s to the early 2000s the steric height in the eastern part of the Irminger Basin increased more rapidly than in the western part, consistent with the evolution of absolute SSH. This suggests that the restratification process leading to the collapse of the lLSW dome was more pronounced on the eastern side of the basin, which is not surprising due to the presence of the buoyant Irminger Current next to the Reykjanes Ridge.

As lLSW formation ceased and the subpolar gyre contracted through the 1990s, increased flow of warm, saline subtropical water into the eastern part of the North Atlantic ensued (Hátún et al., 2005; Sarafanov et al., 2008). This in turn affected the hydrographic properties of the IC. In order to influence the interior Irminger Sea, the Atlantic-origin water must be fluxed from the boundary current. Lateral exchange between the boundary current and the interior, typically in the form of mesoscale eddies, has been extensively investigated in the eastern Labrador Sea (e.g. Lilly et al., 2003; Straneo, 2006). A similar process likely takes place in the eastern Irminger Sea as well. A second mechanism leading to restratification is transport by baroclinic Rossby waves. In the subpolar North Atlantic the internal deformation radius is on the order of 10 km (Chelton et al., 1998). Accordingly, baroclinic Rossby waves would be able to cover the distance between the IC and the IG in less than 10 years. Though we do not see clear evidence of such a westward-propagating signal in the hydrographic data, it could be masked by synoptic variability or the competing effect of a cold, fresh influx along the spreading pathway of LSW from the Labrador Sea. If westward propagation was the primary mechanism of the IG intensification, the assumption of mass balance between the northward and southward branches of the gyre may be called into question. In this case water masses to the southeast of the originally defined northward limb of the gyre may flow northward alongside the gyre but not recirculate within the gyre.

Even though intensification of the IG circulation through a period of diminishing wind stress curl appears paradoxical, there is not necessarily a contradiction between our findings and the model results of Spall and Pickart (2003). Their model gyre was exposed to wind forcing during winter only, yet the circulation was maintained with minimal seasonal variability. An important aspect in this was the slow propagation speed of the baroclinic Rossby waves, which results in a long response time of the Irminger Gyre. As such, one would expect the gyre to start spinning down as it slowly adjusts to the present reduced level of forcing. This needs further investigation, but is beyond the scope of the present study.

A structural change in the deep Irminger Current was observed between the early 1990s and the early 2000s (Fig. 10). In the first pentad there was primarily a single deep extension of the IC located near the crest of the Reykjanes Ridge, while in the latter pentad a second deep extension of the current emerged farther down the ridge near the 2500 m isobath. This latter feature carried the bulk of the deep IC transport in the early 2000s, and was chiefly responsible for the overall increase in full-depth IC transport noted above. Concurrent with the increase in the deep IC transport, the southward flow centered near 520 km in Fig. 10(c) (1991–1995) and near 440 km in Fig. 10(d) (2001–2005) increased as well. If a portion of the IC water were returned southward by this current, the observed positive trend in the deep IC transport may only be a local phenomenon. However, whereas the IG has been mapped using Lagrangian float data (e.g. Lavender et al., 2000), there is no comparable independent evidence of such a recirculation on the eastern side of the Irminger Basin. Although the baroclinic signature of this southward flow is evident, we have not attempted to quantify the transport of this feature.

The hydrographic properties of the two deep IC extensions differ (this is evident in Fig. 9). While still of Atlantic origin, the water transported by the western deep extension is colder and fresher than that in the eastern, which suggests that the two deep extensions have different origins. Such a notion is consistent with synoptic hydrographic surveys of the eastern North Atlantic (e.g. Read, 2001; Pollard et al., 2004) and subsurface float data (Bower et al., 2002). These studies have revealed that there are two distinct pathways from the North Atlantic Current to the Irminger Current. The outer pathway follows the boundary of the subpolar gyre around the rim of the Iceland Basin, while the inner pathway leaves the Iceland Basin shortly after crossing the Mid-

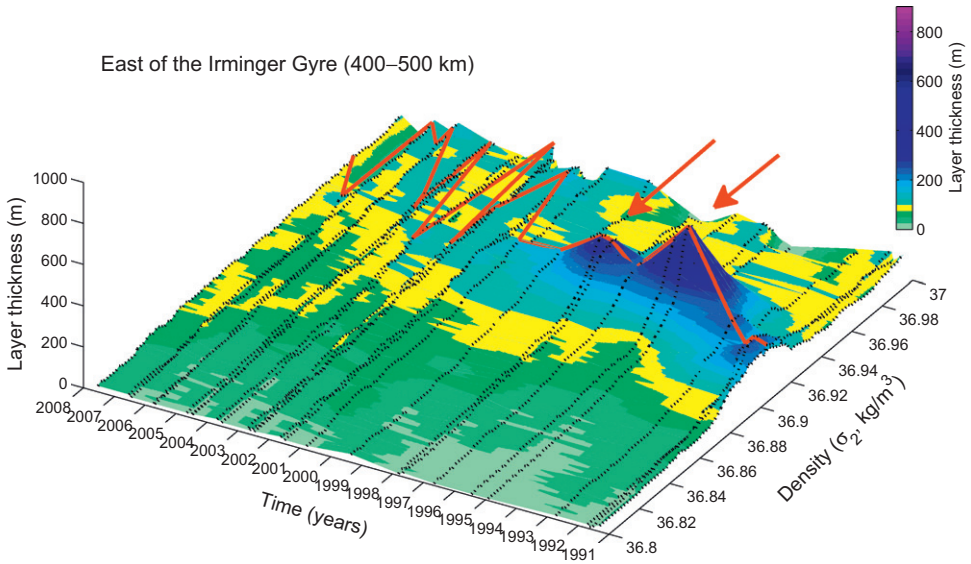

Fig. 22. As Fig. 20, but for the region east of the Irminger Gyre between 400 and 500 km along AR7E. (For interpretation of the references to color in this figure legend, the reader is referred to the web version of this article.)

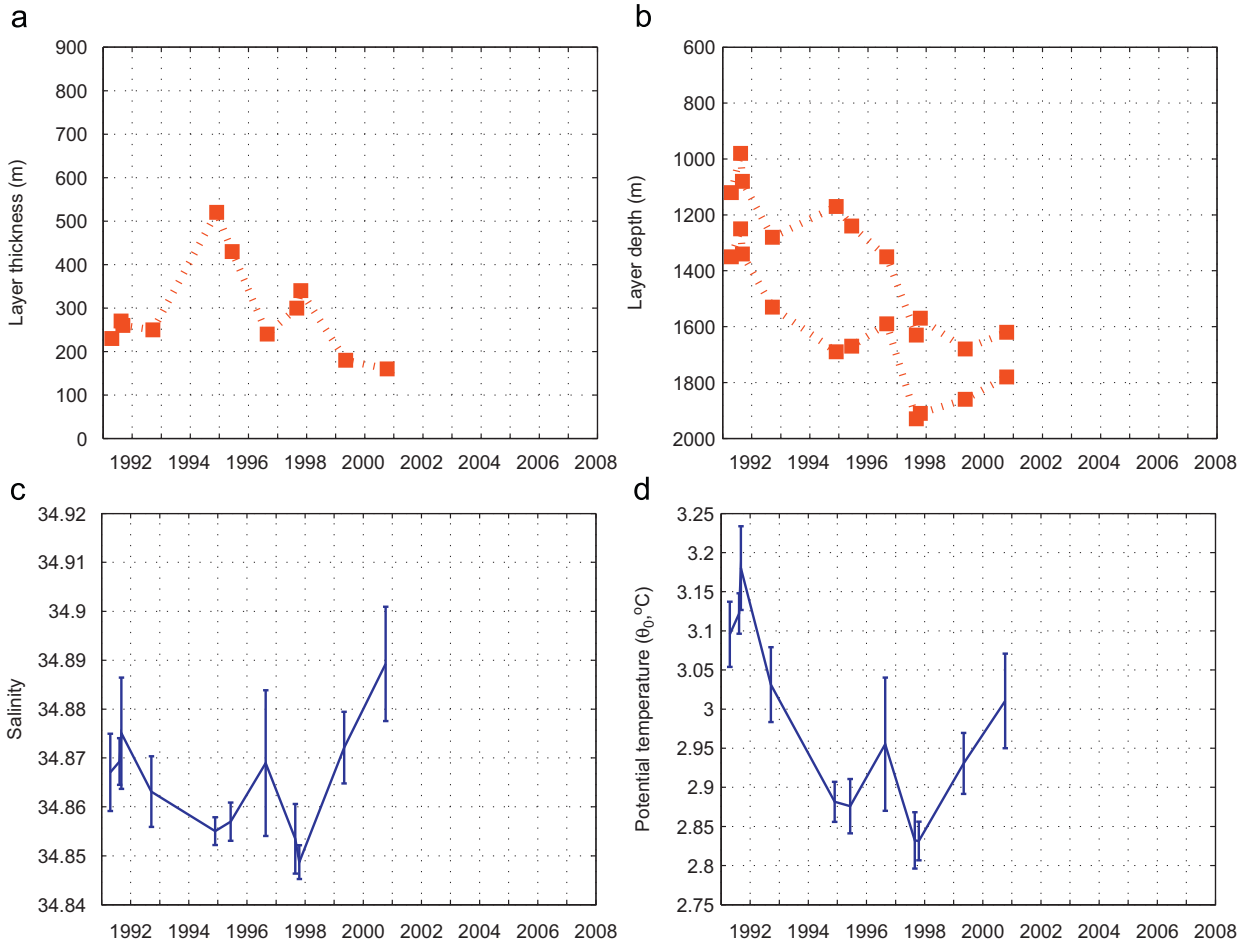

Fig. 23. As Fig. 21, but for the region east of the Irminger Gyre between 400 and 500 km along AR7E. The timeseries were cut before 2001 since reliable detection of the lLSW was no longer feasible (the noisy 2000s signal is evident in Fig. 22).

Atlantic Ridge. Near the southeastern corner of the Irminger Basin the two pathways merge to form the Irminger Current and proceed jointly northwards along the western flank of the Reykjanes Ridge. While both pathways advect subtropical water, the inner pathway also contains an admixture of subpolar water. Using hydrographic data, Pollard et al. (2004) demonstrated that these pathways shifted between 1991 and 1996, apparently due to the contraction of the subpolar gyre. It is reasonable to think

that the relative strengths of these two pathways may change in time as well, and that the increasing flow observed in the western IC extension could be a reflection of the large-scale changes that took place throughout the subpolar gyre from the early 1990s to the early 2000s.

8. Summary and conclusions

In this study we analyzed a collection of 36 hydrographic transects occupied across the southern Irminger Sea between 1991 and 2007. The dramatic changes that took place in the broad subpolar region during this time period are reflected in the Irminger Sea hydrographic data. Most notable is the collapse of the lower LSW dome that reached peak volume in 1995. An EOF analysis identified these changes as the primary mode of variability, and demonstrated a high degree of coherence between the subpolar gyre index of Häkkinen and Rhines (2004, 2009) calculated from North Atlantic SSH levels and the evolution of the local Irminger Sea hydrography.

Using absolute geostrophic velocity sections referenced by satellite altimetry, we quantified for the first time various characteristics of the Irminger Gyre, a closed, cyclonic recirculation in the western Irminger Sea. The mean transport of the gyre was 6.8 ± 1.9 Sv, and over the 17-year study period the transport of the gyre increased at a rate of 3.7 Sv per decade. This increase was associated with a steeper sea level gradient, which is partially due to changes in steric height. In particular, buoyant water, presumably fluxed from the Irminger Current, enhanced the restratification process in the eastern Irminger Basin. This is consistent with the increased presence of subtropical-origin water in the Irminger Current during the second half of the study period, related to the contraction of the subpolar gyre.

Also consistent with the notion of a declining subpolar gyre, the upper-layer transport of the Irminger Current decreased over the study period. However, the full-depth transport of the current increased due to the emergence of a second deep extension of the IC. Relative changes between the two separate pathways that contribute to the IC may have been the cause of this. The mean northward full-depth IC transport was estimated to 19 ± 3 Sv. On the western side of the basin the mean net southward full-depth Western Boundary Current transport was -32 ± 4 Sv (this is the equatorward throughput, as the southward limb of the IG has been subtracted out). For the DWBC (denser than $\sigma_\theta > 27.8$ kg/m^3) we determined a mean net transport of -9.6 ± 1.4 Sv, smaller than the oft-quoted value of Clarke (1984) 13.3 Sv, but more appropriate as a measure of the DWBC contribution to the deep limb of the Meridional Overturning Circulation. Consistent with other studies in both the Irminger and Labrador seas (Dengler et al., 2006; Sarafanov et al., 2009, 2010a), we found that the DWBC transport increased through the study period.

Recognizing the importance of sub-basin scale phenomena in the atmosphere and ocean with regard to convection in the Irminger Sea, we examined the hydrographic data both inside and outside of the Irminger Gyre. We demonstrated that the intermediate salinity maximum purportedly placing a limit on the depth of convection in the Irminger Sea (Bersch et al., 2007) was not continuously present within the IG. Furthermore, we found a single maximum in LSW layer thickness within the IG in 1995, too early to be a remote signal from the Labrador Sea. In contrast, outside of the gyre there were two lLSW layer thickness peaks. The first (in 1994) was likely caused by local convection, while the second (in 1997) is only reconcilable in timing and properties with a remote Labrador Sea source. We believe that our results thus clarify the relative roles of local versus remote convection in contributing to the presence of LSW in the Irminger Sea.

Acknowledgments

We are grateful to Tom Rossby and Svein Østerhus for sharing the Nuka Arctica ADCP data, to Manfred Bersch for sharing hydrographic data, to Kevin Thompson and Simon Higginson for providing the regional ocean topography of the northwest Atlantic, and to Sirpa Häkkinen for providing the updated subpolar gyre index. We thank Norbert Verch and Jan Even Øie Nilsen for assistance with the data assembly. Our analysis benefited from discussions with Julie Deshayes, Mike Spall, Fiamma Straneo, Carl Wunsch, David Fratantoni, Rui Ponte, Guoqi Han, Manfred Bersch, Tatiana Rykova, Femke de Jong, Wilken-Jon von Appen, Beatriz Peña-Molino, and Kevin Thompson. The altimeter products were produced by SSALTO/DUACS and distributed by AVISO, with support from CNES (http://www.aviso.oceanobs.com/duacs/). The GRACE Tellus dynamic ocean topography was obtained from the Jet Propulsion Laboratory (http://grace.jpl.nasa.gov/data/dot/). KV was supported by National Science Foundation (NSF) Grant OCE-0450658. RSP was supported by NSF Grant OCE-0726640. AS was supported by the Russian Ministry of Education and Science under the "World Ocean" Federal Programme (contract 01.420.1.2.0001), the RFBR Grant 11-05-00555, and the Russian President Grant MK 394.2010.5.

Appendix A. Absolute geostrophic velocity errors

It is important to assess the errors associated with the calculation of absolute geostrophic velocities referenced by AVISO surface velocities. The uncertainties originate both from the altimeter and the hydrographic data.

One important difficulty in using altimetry-derived surface velocities as reference values for full-depth geostrophic calculations is the uncertainty of the marine geoid, in particular for areas in the vicinity of land and for scales shorter than about 500 km (e.g. Tapley et al., 2003). In spite of this we found very good correspondence between the 4-year mean surface velocities derived from the geostrophic calculation referenced by direct velocity measurements (ADCP) and the AVISO absolute velocities (Fig. 6). This indicates that, averaged over a sufficient amount of time, the AVISO surface velocities provide a reasonable representation of the directly observed surface flow across the AR7E line. From this comparison we estimate an error associated with the geoid based on the RMS difference between the ADCP-referenced and AVISO geostrophic surface flows. The mean RMS difference is 3.0 cm/s, with the greatest values found over the Greenland shelf and slope and smallest values in the region of the Irminger Gyre. A curve of RMS differences calculated from a running mean filter with a window of 200 km provides an estimate of the uncertainty of the geoid at each nodal point.

Standard errors were computed for each of the summer averaged AVISO reference velocity curves (Fig. 7(a)) using the bootstrap technique, which is a procedure that involves random sampling with replacement from the dataset and does not require any assumptions about the underlying probability distribution. The mean standard error was 1.2 cm/s, and varied between approximately 0.8 cm/s in the WBC and 1.6 cm/s in the IC. The largest standard errors were generally found near the center of the basin and in the IC. We assigned a much larger error to the extrapolated 1991 and 1992 reference velocity curves estimated from the sum of the range and mean standard error of the 1993–1996 curves that served as the basis for the extrapolation.

Density gradients cannot be directly measured below the deepest common level of neighboring hydrographic stations (i.e. the "bottom triangle"). The extrapolation resulting from our Laplacian-spline gridding technique filled these bottom triangles,

but the difference between the extrapolated grid points and the real ocean is unknown. To estimate an error associated with flow through the bottom triangles we first determined the median distance between stations (36 km) and the median slope of the bathymetry over this distance (4.1 m/km) to obtain a "standard bottom triangle area". In the vicinity of steep bathymetry this area would tend to be larger. But, as a matter of routine, station spacing is typically decreased to compensate for the increased bottom triangle area under such conditions, thereby reducing the impact of steep bathymetry on the velocity error. The resulting standard bottom triangle area is equivalent to a uniform layer of thickness 74 m situated directly above the bottom. Combining the standard deviation of the absolute geostrophic velocities within this layer and the area of a standard bottom triangle, we obtain a transport error estimate of 0.18 Sv associated with the data gap. Naturally this error affects only transport estimates of currents extending to the bottom. With a bottom depth of 2300 m (the average depth of the Irminger Basin) and a median distance of 36 km between stations, this error is comparable to a barotropic flow of 0.22 cm/s. For swift, bottom-trapped currents such as the DWBC, the bottom triangles may locally represent a much larger uncertainty. To compensate for this, we have added 0.3 and 1.4 Sv to the total error estimates of the ISOW and DSOW layers, respectively (estimated from the average 0.18 Sv per 36 km bottom triangle error and the mean distance over which each layer is in contact with the bottom).

An error will also result from the projection and gridding. Given the short distance over which most of the stations were projected (82% less than 25 km) we do not expect a significant contribution to the total error resulting from the projection. The error arising from the gridding procedure was estimated from a comparison between the observed data and the gridded data interpolated to the locations of the original observations (e.g. Nikolopoulos et al., 2009). Below 250 m the median RMS difference between actual observations and gridded maps were 0.012 °C and 0.0021 for temperature and salinity, respectively. The temperature RMS difference exceeds the observational error by a factor of 6. In the worst case scenario, where one station would consistently be biased towards colder, saltier conditions by the above RMS differences compared to a neighboring station separated by the median distance of 36 km, the geostrophic velocity error would reach 2 cm/s at 3000 m. This extreme case is highly unrealistic due to the random component of the gridding error. The greatest RMS difference between observed and gridded data occurred on the Greenland shelf, both because of strong gradients in temperature and salinity as well as large differences in the station spacing between the various cruises. This is not an important issue for our study, since the Greenland shelf is not considered.

Finally there is a statistical error associated with use of the synoptic density structure as a proxy for a summertime mean density. This error was estimated in the Labrador Sea by Han and Tang (2001) using historical data at the Ocean Weather Station Bravo site. It was found to be negligible below 1500 m, and responsible for a total uncertainty of about 2.5 Sv in the Labrador Sea WBC. Examination of central Irminger Sea mooring data from the period 2002–2004 (Våge et al., 2008) indicates that the statistical error is non-negligible. A quantitative estimate of this error was obtained using the synoptic sections from years with more than 3 realizations of AR7E (2002–2004, not every section spanned the full width of the Irminger Sea). Absolute velocities were computed from each individual section combined with the annually-averaged AVISO surface velocities as if they were the only section occupied that year, and the transports of the primary features of interest computed for each realization. Subsequently the standard errors of the transports were calculated for each year and then averaged. The resulting estimates of the statistical error are for the WBC: 2.0 Sv; for the DWBC: 1.2 Sv; for the IG: 1.9 Sv; and for the IC: 1.1 Sv. These represent the uncertainty associated with the combination of synoptic hydrography and averaged altimetry. The estimated errors apply to years with single realizations of AR7E, and are reduced for the years when multiple transects are available (by multiplication of the inverse of the square root of the number of transects).

We found above the hydrographic uncertainties to be negligible compared to the errors associated with the temporally averaged AVISO absolute surface velocities that were used for referencing, with the exceptions of the statistical error and the error arising from transport through the bottom triangles for swift, bottom-trapped currents near steep bathymetry (e.g. the DWBC). The total uncertainty of the reference velocity curve for each year was determined as the root of the sum of the squares of the two dominant contributions (geoid and standard errors). The transport errors in Section 5 are estimated from the combined impact of the reference velocity errors and the statistical errors on the geostrophic calculations. Velocities exceeding ± 2 cm/s may in general be considered significant for any pentadal or longer average.

References

Avsic, T., Karstensen, J., Send, U., Fischer, J., 2006. Interannual variability of newly formed Labrador Sea Water from 1994 to 2005. Geophysical Research Letters 33, L21S02. doi:10.1029/2006GL026913.

Bacon, S., 1997. Circulation and fluxes in the North Atlantic between Greenland and Ireland. Journal of Physical Oceanography 27, 1420–1435.

Bacon, S., 1998. Decadal variability in the outflow from the Nordic seas to the deep Atlantic Ocean. Nature 394, 871–873.

Bacon, S., Gould, W.J., Jia, Y.L., 2003. Open-ocean convection in the Irminger Sea. Geophysical Research Letters 30, 1246. doi:10.1029/2002GL016271.

Bacon, S., Reverdin, G., Rigor, I.G., Snaith, H.M., 2002. A freshwater jet on the east Greenland shelf. Journal of Geophysical Research 107, doi:10.1029/2001JC000935.

Bacon, S., Saunders, P.M., 2010. The Deep Western Boundary Current at Cape Farewell: results from a moored current meter array. Journal of Physical Oceanography 40, 815–829. doi:10.1175/2009JPO4091.1.

Bakalian, F., Hameed, S., Pickart, R.S., 2007. Influence of the Icelandic Low latitude on the frequency of Greenland tip jet events: Implications for Irminger Sea convection. Journal of Geophysical Research 112, C04020. doi:10.1029/2006JC003807.

Bendat, J.S., Piersol, A.G., 1986. Random Data: Analysis and Measurement Procedures, second ed. Wiley, New York, NY.

Bersch, M., 1995. On the circulation of the northeastern North Atlantic. Deep-Sea Research 42, 1583–1607.

Bersch, M., Yashayaev, I., Koltermann, K.P., 2007. Recent changes of the thermohaline circulation in the subpolar North Atlantic. Ocean Dynamics 57, 223–235. doi:10.1007/s10236–007–0104–7.

Bower, A.S., Le Cann, B., Rossby, T., Zenk, W., Gould, J., Speer, K., Richardson, P.L., Prater, M.D., Zhang, H.M., 2002. Directly measured mid-depth circulation in the northeastern North Atlantic Ocean. Nature 419, 603–607.

Brambilla, E., Talley, L.D., 2008. Subpolar mode water in the northeastern Atlantic: 1. Averaged properties and mean circulation. Journal of Geophysical Research 113, C04025. doi:10.1029/2006JC004062.

Centurioni, L.R., Gould, W.J., 2004. Winter conditions in the Irminger Sea observed with profiling floats. Journal of Marine Research 62, 313–336.

Chelton, D.B., de Szoeke, R.A., Schlax, M.G., El Naggar, K., Siwertz, N., 1998. Geographical variability of the first baroclinic Rossby radius of deformation. Journal of Physical Oceanography 28, 433–460.

Chelton, D.B., Schlax, M.G., Freilich, M.H., Milliff, R.F., 2004. Satellite measurements reveal persistent small-scale features in ocean winds. Science 303, 978–983.

Clarke, R.A., 1984. Transport through the Cape Farewell—Flemish Cap section. Rapports et Proces-Verbaux des Reunions Conseil Permanent International pour l'exploration de la mer 185, 120–130.

Curry, R., Dickson, R.R., Yashayaev, I., 2003. A change in the freshwater balance of the Atlantic Ocean over the past four decades. Nature 426, 826–829.

de Jong, M.F., 2010. Hydrographic variability of the Irminger Sea. Ph.D. Thesis, University of Utrecht.

Dengler, M., Fischer, J., Schott, F.A., Zantopp, R., 2006. Deep Labrador Current and its variability in 1996–2005. Geophysical Research Letters 33, L21S06. doi:10.1029/2006GL026702.

Dickson, R.R., Brown, J., 1994. The production of North Atlantic Deep Water: sources, rates and pathways. Journal of Geophysical Research 99, 12319–12341.

Dickson, R.R., Rudels, B., Dye, S., Karcher, M., Meincke, J., Yashayaev, I., 2007. Current estimates of freshwater flux through Arctic and subarctic seas. Progress in Oceanography 73, 210–230.
Dickson, R.R., Yashayaev, I., Meincke, J., Turrell, B., Dye, S., Holfort, J., 2002. Rapid freshening of the deep North Atlantic Ocean over the past four decades. Nature 416, 832–837.
Doyle, J.D., Shapiro, M.A., 1999. Flow response to large-scale topography: the Greenland tip jet. Tellus 51, 728–748.
Ducet, N., Traon, P.L., Reverdin, G., 2000. Global high-resolution mapping of ocean circulation from TOPEX/Poseidon and ERS-1 and -2. Journal of Geophysical Research 105, 19477–19498.
Falina, A., Sarafanov, A., Sokov, A., 2007. Variability and renewal of Labrador Sea Water in the Irminger Basin in 1991–2004. Journal of Geophysical Research 112, C01006. doi:10.1029/2005JC003348.
Faure, V., Speer, K., 2005. Labrador Sea Water circulation in the northern North Atlantic. Deep-Sea Research II 52, 565–581.
Flatau, M.K., Talley, L., Niiler, P.P., 2003. The North Atlantic Oscillation, surface current velocities, and SST changes in the subpolar North Atlantic. Journal of Climate 16, 2355–2369.
Fogelqvist, E., Blindheim, J., Tanhua, T., Østerhus, S., Buch, E., Rey, F., 2003. Greenland–Scotland overflow studied by hydro-chemical multivariate analysis. Deep-Sea Research I 50, 73–102.
Fratantoni, P.S., Pickart, R.S., 2007. The western North Atlantic shelfbreak current system in summer. Journal of Physical Oceanography 37, 2509–2533. doi:10.1175/JPO3123.1.
Häkkinen, S., Rhines, P.B., 2004. Decline of subpolar North Atlantic circulation during the 1990s. Science 304, 555–559.
Häkkinen, S., Rhines, P.B., 2009. Shifting surface currents in the northern North Atlantic Ocean. Journal of Geophysical Research 114, C04005. doi:10.1029/2008JC004883.
Han, G., Tang, C.L., 2001. Interannual variations of volume transport in the western Labrador Sea based on TOPEX/Poseidon and WOCE data. Journal of Physical Oceanography 31, 199–211.
Hátún, H., Sandø, A.B., Drange, H., Hansen, B., Valdimarsson, H., 2005. Influence of the Atlantic subpolar gyre on the thermohaline circulation. Science 309, 1841–1844.
Holliday, N.P., Bacon, S., Allen, J., McDonagh, E.L., 2009. Circulation and transport in the western boundary currents at Cape Farewell, Greenland. Journal of Physical Oceanography 39, 1854–1870. doi:10.1175/2009JPO4160.1.
Holliday, N.P., Meyer, A., Bacon, S., Alderson, S.G., de Cuevas, B., 2007. Retroflection of part of the East Greenland Current at Cape Farewell. Geophysical Research Letters 34, L07609. doi:10.1029/2006GL029085.
Hurrell, J.W., 1995. Decadal trends in the North Atlantic Oscillation: regional temperatures and precipitation. Science 269, 676–679.
Johnson, G.C., 2008. Quantifying Antarctic Bottom Water and North Atlantic Deep Water volumes. Journal of Geophysical Research 113, C05027. doi:10.1029/2007JC004477.
Jung, T., Rhines, P.B., 2007. Greenland's pressure drag and the Atlantic storm track. Journal of the Atmospheric Sciences 64, 4004–4030. doi:10.1175/2007JAS2216.1.
Käse, R.H., Biastoch, A., Stammer, D.B., 2001. On the mid-depth circulation in the Labrador and Irminger Seas. Geophysical Research Letters 28, 3433–3436.
Kieke, D., Rhein, M., Stramma, L., Smethie, W.M., Bullister, J.L., LeBel, D.A., 2007. Changes in the pool of Labrador Sea Water in the subpolar North Atlantic. Geophysical Research Letters 34, L06605. doi:10.1029/2006GL028959.
Knudsen, M., 1899. Hydrography. Danish Ingolf expedition. Bd. 1, No. 2. Copenhagen.
Knutsen, Ø., Svendsen, H., Østerhus, S., Rossby, T., Hansen, B., 2005. Direct measurements of the mean flow and eddy kinetic energy structure of the upper ocean circulation in the NE Atlantic. Geophysical Research Letters 32, L14604. doi:10.1029/2005GL023615.
Kvaleberg, E., Haine, T.W.N., Waugh, D.W., 2008. Middepth spreading in the subpolar North Atlantic Ocean: reconciling CFC-11 and float observations. Journal of Geophysical Research 113, C08019. doi:10.1029/2007JC004104.
Lavender, K.L., Davis, R.E., Owens, W.B., 2000. Mid-depth recirculation observed in the interior Labrador and Irminger Seas by direct velocity measurements. Nature 407, 66–69.
Lavender, K.L., Owens, W.B., Davis, R.E., 2005. The mid-depth circulation of the subpolar North Atlantic Ocean as measured by subsurface floats. Deep-Sea Research I 52, 767–785.
Lazier, J.R.N., Hendry, R., Clarke, R.A., Yashayaev, I., Rhines, P.B., 2002. Convection and restratification in the Labrador Sea, 1990–2000. Deep-Sea Research I 49, 1819–1835.
Le Traon, P.Y., Faugére, Y., Hernandez, F., Dorandeu, J., Mertz, F., Ablain, M., 2003. Can we merge GEOSAT Follow-On with TOPEX/Poseidon and ERS-2 for an improved description of the ocean circulation? Journal of Atmospheric and Oceanic Technology 20, 889–895.
Lherminier, P., Mercier, H., Gourcuff, C., Alvarez, M., Kermabon, C., 2007. Transports across the 2002 Greenland–Portugal Ovide section and comparison with 1997. Journal of Geophysical Research 112, C07003. doi:10.1029/2006JC003716.
Lherminier, Mercier, H., Huck, T., Gourcuff, C., Perez, F.F., Morin, P., Sarafanov, A., 2010. The Atlantic Meridional Overturning Circulation and the subpolar gyre observed at the A25-OVIDE section in June 2002 and 2004. Deep-Sea Res. I 57, 1374–1391. doi:10.1016/j.dsr.2010.07.009.
Lilly, J.M., Rhines, P.B., Schott, F., Lavender, K., Lazier, J.R.N., Send, U., D'Asaro, E.A., 2003. Observations of the Labrador Sea eddy field. Progress in Oceanography 59, 75–176.
McCartney, M.S., Talley, L.D., 1982. The subpolar mode water of the North Atlantic Ocean. Journal of Physical Oceanography 12, 1169–1188.
Mesinger, F., DiMego, G., Kalnay, E., Mitchell, K., Shafran, P.C., et al., 2006. North American regional reanalysis. Bulletin of the American Meteorological Society 87, 343–360.
Milliff, R.F., Morzel, J., 2001. The global distribution of the time-average wind stress curl from NSCAT. Journal of the Atmospheric Sciences 58, 109–131.
Moore, G.W.K., Renfrew, I.A., 2005. Tip jets and barrier winds: a QuikSCAT climatology of high wind speed events around Greenland. Journal of Climate 18, 3713–3725.
Nikolopoulos, A., Pickart, R.S., Fratantoni, P.S., Shimada, K., Torres, D.J., Jones, E.P., 2009. The western Arctic boundary current at 152°W: structure, variability, and transport. Deep-Sea Research II 56, 1164–1181. doi:10.1016/j.dsr2.2008.10.014.
Pickart, R.S., 2004. Shelfbreak circulation in the Alaskan Beaufort Sea: mean structure and variability. Journal of Geophysical Research 109, C04024. doi:10.1029/2003JC001912.
Pickart, R.S., McKee, T.K., Torres, D.J., Harrington, S.A., 1999. Mean structure and interannual variability of the slopewater system south of Newfoundland. Journal of Physical Oceanography 29, 2541–2558.
Pickart, R.S., Smethie, W.M., 1998. Temporal evolution of the Deep Western Boundary Current where it enters the subtropical domain. Deep-Sea Research I 45, 1053–1083.
Pickart, R.S., Spall, M.A., Ribergaard, M.H., Moore, G.W.K., Milliff, R.F., 2003a. Deep convection in the Irminger Sea forced by the Greenland tip jet. Nature 424, 152–156.
Pickart, R.S., Straneo, F., Moore, G.W.K., 2003b. Is Labrador Sea water formed in the Irminger Basin? Deep-Sea Research I 50, 23–52.
Pickart, R.S., Torres, D.J., Fratantoni, P.S., 2005. The East Greenland Spill Jet. Journal of Physical Oceanography 35, 1037–1053.
Pollard, R.T., Read, J.F., Holliday, N.P., Leach, H., 2004. Water masses and circulation pathways through the Iceland Basin during Vivaldi 1996. Journal of Geophysical Research 109, C04004. doi:10.1029/2003JC002067.
Read, J.F., 2001. CONVEX-91: water masses and circulation of the Northeast Atlantic subpolar gyre. Progress in Oceanography 48, 461–510.
Rio, M.H., Hernandez, F., 2004. A mean dynamic topography computed over the world ocean from altimetry, in situ measurements, and a geoid model. Journal of Geophysical Research 109, C12032. doi:10.1029/2003JC002226.
Rogers, J.C., 1990. Patterns of low-frequency monthly sea level pressure variability (1899–1986) and associated wave cyclone frequencies. Journal of Climate 3, 1364–1379.
Sarafanov, A., 2009. On the effect of the North Atlantic Oscillation on temperature and salinity of the subpolar North Atlantic intermediate and deep waters. ICES Journal of Marine Science 66, 1448–1454.
Sarafanov, A., Falina, A., Lherminier, P., Mercier, H., Sokov, A., Gourcuff, C., 2010a. Assessing decadal changes in the Deep Western Boundary Current absolute transport southeast of Cape Farewell, Greenland, from hydrography and altimetry. Journal of Geophysical Research 115, C11003. doi:10.1029/2009JC005811.
Sarafanov, A., Falina, A., Mercier, H., Lherminier, P., Sokov, A., 2009. Recent changes in the Greenland–Scotland overflow-derived water transport inferred from hydrographic observations in the southern Irminger Sea. Geophysical Research Letters 36, L13606. doi:10.1029/2009GL038385.
Sarafanov, A., Falina, A., Sokov, A., Demidov, A., 2008. Intense warming and salinification of intermediate waters of southern origin in the eastern subpolar North Atlantic in the 1990s to mid-2000s. Journal of Geophysical Research 113, C12022. doi:10.1029/2008JC004975.
Sarafanov, A., Mercier, H., Falina, A., Sokov, A., Lherminier, P., 2010b. Cessation and partial reversal of deep water freshening in the northern North Atlantic: observation-based estimates and attribution. Tellus 62A, 80–90.
Sarafanov, A., Sokov, A., Demidov, A., Falina, A., 2007. Warming and salinification of intermediate and deep waters in the Irminger Sea and the Iceland Basin in 1997–2006. Geophysical Research Letters 34, L23609. doi:10.1029/2007GL031074.
Spall, M.A., Pickart, R.S., 2003. Wind-driven recirculations and exchange in the Labrador and Irminger Seas. Journal of Physical Oceanography 33, 1829–1845.
Straneo, F., 2006. Heat and freshwater transport through the central Labrador Sea. Journal of Physical Oceanography 36, 606–628.
Straneo, F., Pickart, R.S., Lavender, K.L., 2003. Spreading of Labrador Sea Water: an advective-diffusive study based on Lagrangian data. Deep-Sea Research I 50, 701–719.
Sutherland, D.A., Pickart, R.S., 2008. The East Greenland Coastal Current: structure, variability and forcing. Progress in Oceanography 78, 58–77. doi:10.1016/j.pocean.2007.09.006.
Talley, L.D., McCartney, M.S., 1982. Distribution and circulation of Labrador Sea Water. Journal of Physical Oceanography 12, 1189–1205.
Tapley, B.D., Chambers, D.P., Bettadpur, S., Ries, J.C., 2003. Large scale ocean circulation from the GRACE GGM01 geoid. Geophysical Research Letters 30, doi:10.1029/2003GL018622.
Thompson, K.R., Huang, J., Véronneau, M., Wright, D.G., Lu, Y., 2009. Mean surface topography of the northwest Atlantic: comparison of estimates based on satellite, terrestrial gravity, and oceanographic observations. Journal of Geophysical Research 114, C07015. doi:10.1029/2008JC004859.
Våge, K., Pickart, R.S., Moore, G.W.K., Ribergaard, M.H., 2008. Winter mixed-layer development in the central Irminger Sea: the effect of strong, intermittent wind events. Journal of Physical Oceanography 38, 541–565.

Våge, K., Pickart, R.S., Thierry, V., Reverdin, G., Lee, C.M., Petrie, B., Agnew, T.A., Wong, A., Ribergaard, M.H., 2009a. Surprising return of deep convection to the subpolar North Atlantic Ocean in winter 2007–2008. Nature Geoscience 2, 67–72. doi:10.1038/NGEO382.

Våge, K., Spengler, T., Davies, H.C., Pickart, R.S., 2009b. Multi-event analysis of the westerly Greenland tip jet based upon 45 winters in ERA-40. Quarterly Journal of the Royal Meteorological Society 135, 1999–2011. doi:10.1002/qj.488.

van Aken, H.M., de Boer, C.J., 1995. On the synoptic hydrography of intermediate and deep water masses in the Iceland Basin. Deep-Sea Research 42, 165–189.

Wilcoxon, F., 1945. Individual comparisons by ranking methods. Biometrics Bulletin 1, 80–83.

Yashayaev, I., 2007. Hydrographic changes in the Labrador Sea, 1960–2005. Progress in Oceanography 73, 242–276.

Yashayaev, I., Bersch, M., van Aken, H.M., 2007a. Spreading of the Labrador Sea Water to the Irminger and Iceland basins. Geophysical Research Letters 34, L10602. doi:10.1029/2006GL028999.

Yashayaev, I., van Aken, H.M., Holliday, N.P., Bersch, M., 2007b. Transformation of the Labrador Sea Water in the subpolar North Atlantic. Geophysical Research Letters 34, L22605. doi:10.1029/2007GL031812.